Summary of the Second High-Altitude, Supersonic Flight Dynamics Test for the LDSD Project

Dr. Ian Clark
Jet Propulsion Laboratory
California Institute of Technology
Pasadena, CA 91109
ian.g.clark@jpl.nasa.gov

Dr. Mark Adler
Jet Propulsion Laboratory
California Institute of Technology
Pasadena, CA 91109
mark.adler@jpl.nasa.gov

***Abstract*—NASA's Low-Density Supersonic Decelerator Project is developing and testing the next generation of supersonic aerodynamic decelerators for planetary entry. A key element of that development is the testing of full-scale articles in conditions relevant to their intended use, primarily in the tenuous Mars atmosphere. To achieve this testing, the LDSD project developed a new test architecture for the qualification of their supersonic parachute. A large, helium filled scientific balloon is used to hoist a 4.7 m blunt body test vehicle to an altitude of approximately 32 kilometers. The test vehicle is released from the balloon, spun up for gyroscopic stability, and accelerated to over four times the speed of sound and an altitude of 50 kilometers using a large solid rocket motor. Once at those conditions, the vehicle is despun and the test period begins.**

The second flight of this architecture occurred on June 8th, 2015. This flight sought to build on the very successful shakeout test of 2014 by testing an updated design of a new 30.5 meter nominal diameter supersonic parachute that applied lessons learned from the first flight. Two other supersonic decelerators were also tested: a 6 m diameter Supersonic Inflatable Aerodynamic Decelerator (SIAD), and a 4.4 m diameter trailing ballute. This paper summarizes the results from that test.

Table of Contents

1 Introduction 1
2 Technology Overview 2
3 Instrumentation 4
4 Mission Operations 5
5 Atmosphere & Test Conditions 8
6 SIAD-R Performance 9
7 Parachute Deployment Device 16
8 Supersonic Ringsail Parachute 19
9 Summary 23
Acknowledgments 23
References 23
Biography 24

1. Introduction

In 1976, the twin Viking spacecraft became the first spacecraft to successfully land on the surface of Mars. The technology set utilized by Viking, namely a rigid blunt body aeroshell, a supersonic parachute, and a propulsion-based terminal descent system, is largely the same one used in the subsequent four decades of Mars spacecraft. Although numerous improvements have been made in the area of hypersonic guidance and terminal descent systems, the supersonic parachute used by Viking is still used consistently. With the successful landing of the Mars Science Laboratory Curiosity rover, it is likely that the landed mass and altitude capabilities of the Viking heritage supersonic decelerator is saturated. Future missions seeking to land greater mass or access higher altitudes will require new supersonic decelerators.

In 2011, NASA initiated the Low-Density Supersonic Decelerator (LDSD) project to develop a new generation of supersonic aerodynamic decelerators. As part of the LDSD project, several new ground-based test architectures were developed for performing structural testing of the decelerators. However, to fully evaluate deployment, inflation, and supersonic and subsonic aerodynamic behaviors, a full-scale flight test was required at conditions relevant to how the technologies would be utilized at Mars. This test series, referred to as the Supersonic Flight Dynamics Test (SFDT), utilizes a test architecture (Figure 1) similar to that of the Viking Balloon Launched Decelerator Test (BLDT) series of 1972.

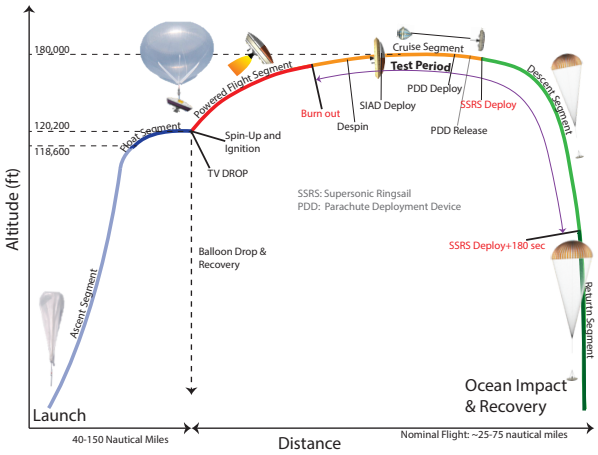

Figure 1. Overview of the LDSD Supersonic Flight Dynamics Test architecture

For a nominal mission, a large helium balloon is used to hoist a 4.7 m diameter blunt body test vehicle to an altitude of over 36 km. The test vehicle is released from the balloon, spun-up for stability, and a Star-48 solid rocket motor is ignited. The motor accelerates the test vehicle to approximately Mach 4 and an altitude of 50 km. Upon burn-out, the vehicle is despun and the primary test phase begins. Shortly thereafter, the first of the technologies, a Supersonic Inflatable Aerody-

978-1-4799-5380-6/15/$31.00 ©2015 California Institute of Technology. Government sponsorship acknowledged.

namic Decelerator (SIAD) is deployed. Later in the flight, the Parachute Deployment Device (PDD) is mortar fired, inflated, and subsequently used as a pilot device to extract and deploy a large supersonic parachute from the test vehicle. The parachute then decelerates the vehicle to subsonic conditions and the vehicle descends to the ocean for recovery.

The second of these tests, SFDT-2, was conducted on June 8th of 2015 with a balloon launch from the Pacific Missile Range Facility in Hawaii. This paper provides documentation of the results of the second test, including balloon launch and float, flight and performance of the SFDT-2 test vehicle, and performance of the technologies tested. Data relevant to these items is presented throughout the paper. A summary of the first flight, SFDT-1, can be found in Reference [1].

Test Objectives

The first SFDT flight occurred in June of 2014 and was intended as a shakeout flight of the overall test architecture though both the SIAD-R and a supersonic parachute were tested at that time. The performance of SIAD-R during SFDT-1 was considered to be adequate to achieve the investigation goals associated with SIAD-R and no further supersonic tests were required. However, the parachute did not perform as hoped and subsequent supersonic flights would be required. Thus, the objectives of the second SFDT flight were focused on achieving a good test of a large supersonic parachute. The minimum success criteria established were as follows:

1. Deliver a flight-like 30 m D_0 or larger supersonic parachute to the required test conditions at line stretch behind a 6 m diameter blunt forebody.
2. Collect real-time telemetry from the test vehicle or recover data from the on-board recorder and collect coincident high-altitude atmosphere data, which in combination are sufficient to reconstruct the trajectory and determine the deployment conditions, total force, and flight dynamics of the parachute through three minutes after PDD bridle cut.
3. Collect both high-speed and high-resolution video over the three minutes following PDD bridle cut to observe and measure deployment, inflation, integrity, and flight dynamics of the parachute.
4. Recover the balloon envelope from the ocean for disposal.

The minimum success criteria define what was necessary to achieve a good test of the supersonic parachute and the data needed from that test. Additional criteria were defined to constitute a "full-success" of the flight. These were:

- Collect data on SIAD-R deployment, inflation, and flight dynamics.
- Maintain general parachute integrity through three minutes after PDD bridle cut.
- Recover and return the test vehicle and parachute.

Modifications From SFDT-1

Following SFDT-1, LDSD incorporated a number of changes for SFDT-2. The primary changes fall in to three categories: operations, instrumentation, and technologies. On the operations side, two primary changes made were:

- Incorporated sun-angle predictions into the launch procedures. Depending on the time of balloon launch and test vehicle release, different launch azimuths would be more favorable for ensuring that the sun would not over expose camera instrumentation. Predictions of the sun angle were made prior to the day of launch and updated throughout balloon ascent and float to optimize the desired launch azimuth of the test vehicle.
- Modified the triggering approach to better achieve targeted test conditions. The trajectory flown during SFDT-1 was higher than anticipated due to differences in the atmosphere, Star-48 performance, and estimates of the test vehicle aerodynamics during powered flight. A change was made to the triggering software to adjust the velocity triggers based on a calculated altitude at Star-48 burnout.

On the instrumentation side, changes were made to acquire better measurements of the parachute's performance at the expense of some data specific to the SIAD's performance. These changes included:

- Addition of an extra high-resolution (HR) and high-speed (HS) uplook camera. The high speed camera previously used to acquire a panoramic view of SIAD inflation was retasked as an uplook camera. An additional HR camera was also added to the camera mast assembly. Furthermore, a camera triggering change was included that enabled the cameras to take images out of phase of one another, effectively doubling the high-resolution and high-speed frame rates achieved.
- Removal of the internal SIAD camera. To allow for the inclusion of the second HR camera, the internal camera was disconnected from the flight image recorder.
- Addition of two more situational awareness uplook cameras. These two cameras were placed on opposite sides of the top deck of the vehicle. The cameras were primarily used as a proof of concept for stereo imagery and three-dimensional reconstruction of the parachute geometry.
- Addition of a pressure transducer to measure Star-48 chamber pressure. Though flown on SFDT-1, the Star-48 pressure transducer was left disconnected due to a concern about shorting of the harness. This was rectified for SFDT-2 and data was taken during flight.
- Addition of two base pressure transducers to measure the aft body pressure during powered flight and cruise. These sensors were intended to provide additional data for validating computational aerodynamic analyses and to provide early data on potential instrumentation for future Mars missions.

Lastly, the parachute configuration was changed from the Disksail design flown on SFDT-1 to a Ringsail design.

2. TECHNOLOGY OVERVIEW

The Low-Density Supersonic Decelerator (LDSD) Project is developing three new aerodynamic decelerators that are targeted for use in future Mars missions. Two of these devices are supersonic inflatable aerodynamic decelerators (SIADs) and the third is a new supersonic parachute. Each of the two SIADs is named for the class of mission for which it is envisioned to be used for, either robotic class missions (SIAD-R) or exploration class missions (SIAD-E). As a combined SIAD/parachute system, these technologies will allow for increases in landed mass, landed altitude, and landed accuracy beyond what is presently possible with the heritage set of decelerator technologies.

A SIAD is a class of aerodynamic decelerator that is intended to alter the aerodynamic characteristics of an entry vehicle, typically by augmenting drag or lift and/or improving the stability of the entry vehicle. Since they are inflated structures, SIADs provide benefits in mass and packaging and allow for increases in the aerodynamic surfaces of an entry vehicle beyond those provided by a rigid aeroshell constrained to fit within a launch vehicle fairing. As a supersonic decelerator,

they are deployed well after the peak heating and deceleration phase but at Mach numbers above those for which parachutes can be used. In that manner, they provide a bridge from hypersonic entry to a Mach and dynamic pressure regime in which a parachute may be used.

SIAD-R

The robotic class SIAD consists of an inflated torus with a total diameter of 6 m. The design of SIAD-R is intended to provide an inflated structure that can be pressurized sufficiently to exhibit little or no change in shape when operating in a supersonic flowfield. This feature greatly simplifies the qualification and testing that would be necessary prior to incorporation on a flight mission. For example, since SIAD-R behaves as a rigid structure, aerodynamic characterization can still be performed using traditional techniques that assume rigidity like CFD, subscale wind tunnel testing, and ballistic range testing.

Though primarily an inflated torus, the SIAD-R design has a number of features, shown in Figure 2, designed to improve performance and rigidity. The burble fence on the periphery of the SIAD provides a location of uniform flow separation that improves the stability of the vehicle, particularly at lower supersonic and transonic conditions. The primary torus also contains a series of internal cords that provide additional preload and stiffness in the structure and help resist axial deflection and rotation of the torus under large aerodynamic loads.

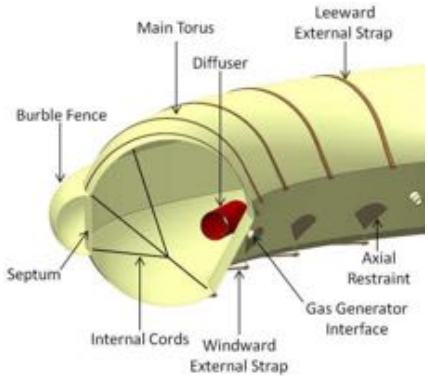

Figure 2. Design features of the robotic class SIAD flown on SFDT-1.

The SIAD is constructed primarily from 400-denier Kevlar-29 as the woven broadcloth material with a coating of Silicone RTV. The structure is fabricated using 27 gores sewn together to approximate a circular cross-section. Inflation of SIAD-R is achieved using an on-board inflation system of 18 gas generators (gg's). The gas generators are fired in two separate groups, an initial lower pressure firing and a subsequent high pressure firing. The low pressure firing uses 9 gas generators consisting of canisters of nitrogen pressurized to approximately 6 kPa (0.87 psi), while the high pressure firing uses combustion products. The gas generators are installed in pairs, with low and high pressure paired in 40° intervals around the vehicle.

To achieve its rigidity, the SIAD is pressurized to a peak inflation pressure of approximately 31 kPa (4.5 psi). The relatively small size of the SIAD also allows for a rapid inflation of less than one second, thereby minimizing disturbances on the vehicle.

The SIAD-R used in SFDT-2 was Unit 2A. This was the first production SIAD fabricated for supersonic testing but during acceptance testing an anomalous geometry was observed in the form of a waviness in the burble fence from gore to gore. Aerodynamic analyses conducted on a high resolution laser scanned geometry indicated that the effect of the geometry variances would be negligible to the overall aerodynamics. Thus, the unit was cleared for flight on SFDT-2.

Supersonic Ringsail Parachute

The parachute tested on SFDT-2 was a 96 gore, 30.5 m D_0 Supersonic Ringsail (SSRS), shown in Figure 3. Failure of the Disksail design on SFDT-1 led to a change in canopy configuration back to a more classical Ringsail design. The design is a 20 panel, 96-gore canopy with quarter-spherical constructed geometry. The first five panels of a gore are rings with 0% fullness. Panels 6-12 are sails with 6% fullness and panels 13-19 are sails with 12% fullness. Panel 20 contains zero fullness, as per typical Ringsail design. Two gaps are present, one large gap between panels 9 and 10 and another shorter gap between the 15th and 16th panels. The parachute has an as-designed geometric porosity of 14.9%, though the as-built geometric porosity of the canopy tested was estimated as 15.2%.

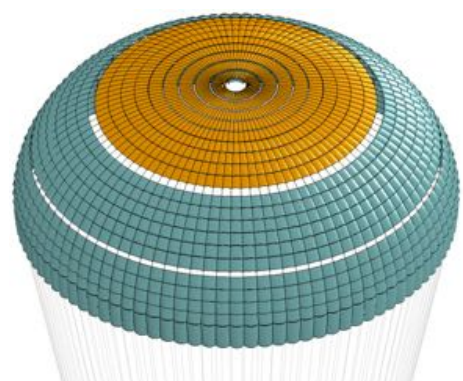

Figure 3. Supersonic Ringsail parachute flown on SFDT-2.

Construction of the parachute utilizes Kevlar for the radial and circumferential skeleton. Upper rings and sails, specifically panels 1-9, incorporated circumferentials on both the leading and trailing edges of the parachute while lower portions only had circumferentials on the trailing edge of the canopy. A combination of 800 lbf (PIA-T-87130, Type I, Class 3) and 550 lbf (PIA-T-87130, Type I, Class 2), 0.5 in wide tapes were used. The 800 lbf tapes were used on the trailing edge of panels 2-12 and the leading edge of panels 1-5 while the 550 lbf tapes were used on the trailing edge of panels 13-20 and the leading edge of panels 6-9. The radial tapes and skirt band were constructed from 2500 lbf, 1 in wide Kevlar tape (PIA-T-87130, Type VI, Class 6). The 96 suspension lines and 48 vent lines were each 2100 lbf Technora cord. The vent band was a 6000 lbf Nylon webbing.

Two separate Nylon materials were used for the broadcloth. The upper portion of the canopy, panels 1-9, was constructed from 1.9 oz/yd^2 Diamond Weave ripstop Nylon, with a minimum specified strength of 80 lbf/in in the warp direction and 85 lbf/in in the fill direction. The lower portion of the canopy, below the upper gap, was constructed from 1.2 oz/yd^2 PIA-

C-44378 Type I ripstop Nylon with a minimum specified strength of 45 lbf/in. Low or zero-permeability materials were intentionally selected for parachute construction. The nominal permeability of PIA-C-44378 is 0-5 cfm while the Diamond Weave permeability is 20-50 cfm. Because of this, the total porosity, including the effects of material permeability, of the Ringsail should be close to the geometric porosity.

The parachute was packed in a two stage deployment bag, with the canopy and approximately 8 m of suspension lines packed into an inner bag and the remainder of the suspension lines packed into an outer bag. The achieved density of the pack was estimated as 597.4 kg/m^3 (37.3 lbm/ft^3). After deployment, the inner bag remained attached to the parachute vent lines while the outer bag remained with the ballute.

Parachute Deployment Device

Although it was not one of the primary technologies being tested by LDSD, deployment of the SSRS required development of a trailing ballute Parachute Deployment Device (PDD), shown in Figure 4 below. The ballute served as a supersonic pilot device to extract the parachute off of the back of the test vehicle. The basic design was of a 16 gore, 4.4 m diameter, trailing isotensoid of a design similar to prior ballutes tested by NASA (e.g. [2],[3]).

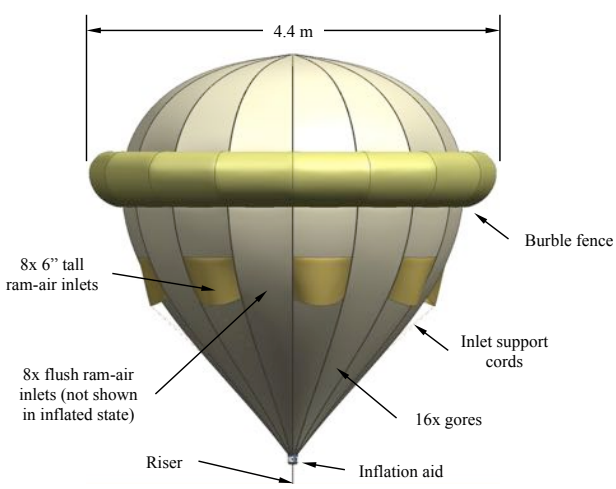

Figure 4. Ballute Parachute Deployment Device used on SFDT-2.

The geometry of the ballute included a 10% burble fence such that the core diameter of the isotensoid was 4.0 m but inclusion of the burble fence increased the total diameter to 4.4 m. The burble fence is a feature historically common to ballutes that provides a clean separation point and improves stability of the device.

The ballute was designed such that primary inflation is achieved through the use of ram-air inlets. However, an inflation aid device [4] was also incorporated into the ballute design to reduce the risk of failed inflation, such as that observed on a prior NASA test of a 5.49 m diameter ballute [2]. The inflation aid consisted of a water/methanol mixture and was sized to provide at least half of the expected inflation pressure, depending on the conditions of deployment. The ballute was built with 16 ram-air inlets, one on each gore, of two different designs. Every other gore of the ballute had an inlet that stood approximately 15.24 cm off of the surface of the ballute while the remaining half of the inlets were flush-mounted (e.g. zero fullness) with the curvature of the ballute. If the ballute was not fully pressurized, the flush-mounted inlets would serve to provide additional inlet area to facilitate inflation. Tethers attached to the leading edge of each of the raised inlets were used to ensure that the inlets would not fold back.

The ballute broadcloth was a plain 60 x 60 weave, 200 denier Kevlar 29 cloth with a thin coating of clear KS-1100T Silicone. The uncoated areal density of the broadcloth was measured as 3.14 oz/yd^2 and the coated areal density was 4.17 oz/yd^2. Meridian tapes of 625 lbf Kevlar were used as reinforcement. A trailing distance of 42 m from the maximum diameter of the deployed SIAD-R to the nose of the ballute was achieved using a combination of 5.5 m long triple bridle legs and a roughly 36.5 m long riser. The riser was a 12,500 lbf Kevlar web (PIA-87130 Type VI, Class 11, 1 in. wide) and the triple bridle legs were two legs of 7000 lbf Kevlar webbing (PIA-87130 Type VI Class 9a, 1 in. wide) and a leg of 12,500 lb Kevlar webbing. Attached to the stronger of the three bridle legs was a lazy leg connected to the parachute pack. When the ballute triple bridle is cut, the lazy leg extracts the parachute pack from the back of the vehicle.

The ballute and inflation aid were packed into a single deployment bag with an estimated packing density of 661.6 kg/m^3 (41.3 lbm/ft^3).

3. INSTRUMENTATION

The SFDT-2 Test Vehicle (TV) was equipped with scientific instrumentation to observe the trajectory, aerodynamics, and performance of both the test vehicle and test articles. Tabular descriptions of the metric and imagery instrumentation accuracy and specifications are shown in Tables 1 and 2. Image resolution accuracies for the high-speed and high-resolution cameras were estimated as 2.27 cm/pixel and 1.18 cm/pixel at a distance of 70 m, respectively.

Table 1. Metric Instrumentation Summary

Device	Sample Rate	Location
GLN-MAC IMU	400 Hz	
Javad G2T GPS	10 Hz	
SIAD Surface Thermocouples	50 Hz	Gores 2, 11, 20 †‡
SIAD Internal Gas Thermocouples	50 Hz	Gores 2, 11, 20 †
SIAD Internal Pressure Transducers	1 kHz	Gores 2, 11, 20 †
SIAD Leeward Load Cells	1 kHz	Gores 2, 11, 20 †
PDD Load Cells	1 kHz	PDD Bridle Legs
SSDS Load Cells	1 kHz	SSDS Bridle Legs

† See Figure 5 for the SIAD gore labels
‡ See Figure 6 for the surface SIAD thermocouple configuration

Table 2. Imagery Instrumentation Summary

Camera	Location	FOV
High-Speed (x2), 135 fps	Camera mast, aft-pointed	38°x38°
High-Res (x2), 16 fps	Camera mast, aft-pointed	48°x37°
Situational Video 1, 30 fps	Top deck, center-pointed	69.5°x118.2°
Situational Video 2, 30 fps	Camera mast, +X pointed	69.5°x118.2°
Situational Video 3, 30 fps	Camera mast, -X pointed	69.5°x118.2°
Situational Video 4, 30 fps	Camera mast, aft-pointed	69.5°x118.2°
Stereo Video (x2), 60 fps	Top deck, aft-pointed	37°x37°

Inertial Measurement Unit

The SFDT-2 Test Vehicle (TV) flew one inertial measurement unit, a Gimbaled LN-200 with Miniature Airborne Computer (GLN-MAC) which also provided in-flight navigated velocity for the purpose of triggering. The GLN-MAC has a single gimbal that is approximately aligned with the roll axis of the TV. This allows the internal LN-200 to stay primarily inertially fixed during the powered phase of the flight, while the vehicle rotates around it at approximately 300 degrees per second during powered flight. The GLN-MAC provides the following data at 400 Hz that is used directly in trajectory and aerodynamic reconstruction: rotational delta-thetas from the gyroscopes about the LN-200 X, Y, and Z instrument axes, translational delta-velocities from the accelerometers in the LN-200 X, Y, and Z instrument axes, and the gimbal position about the GLN-MAC X platform axis.

GPS Unit

The SFDT-2 TV flew one GPS unit, a Javad G2T, with two diametrically opposed antennas, mounted on the shoulder of the vehicle. It was predicted that the GPS would lose lock of the satellites during the powered spin phase of the flight, where the vehicle was expected to spin at approximately 300 deg/s. During the spin phase, the GPS unit did lose lock, but regained it within a few seconds of spinning down.

The final flight trajectory filter used the in-flight performance of the unit to estimate output uncertainties.

SIAD Instrumentation

SIAD Surface Thermocouples—The 21 surface thermocouples were grouped in sets of 7 thermocouples, located at three circumferential locations on the SIAD, at gores 2, 11, and 20. See Figure 5 for the gore configuration and numbering scheme. At each gore, the thermocouples were installed in a consistent configuration, as shown in Figure 6.

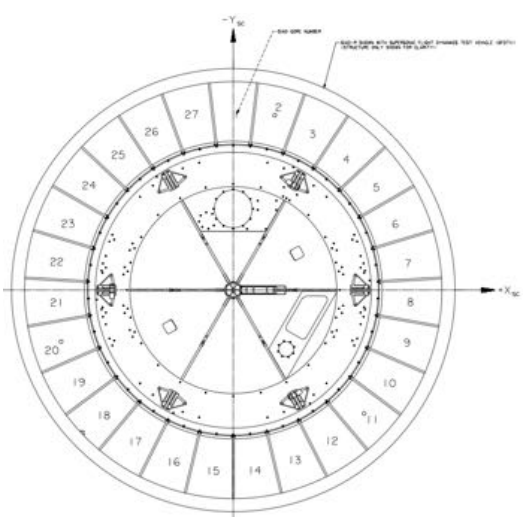

Figure 5. SIAD gore configuration

SIAD Internal Gas Thermocouples—The 3 internal gas thermocouples were located at the same gores as the surface thermocouples: gores 2, 11, and 20, as shown in Figure 5. Due to construction of the SIAD and thermocouple mounting, these may not be reading the true gas temperature, and may have been sensing some surface conductive heating.

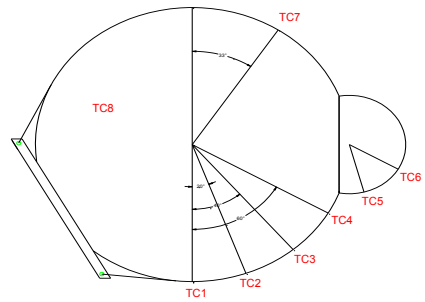

Figure 6. SIAD thermocouples in the same configuration at each gore

SIAD Internal Pressure Transducers—The 3 internal pressure transducers were located at the same gores as the thermocouples: gores 2, 11, and 20.

Parachute Instrumentation

PDD Load Cells—The 3 triple-bridle PDD load cells were located in line with the three triple bridles, near the triple-bridle and top deck interface. Each load cell had a range of 1kN to 4kN, at a frequency of 1 kHz, and an accuracy of 600 N.

SSDS Load Cells—The 3 triple-bridle SSDS load cells were located in line with the three triple bridles, near the triple-bridle and top deck interface. Each load cell had a range of 5kN to 267kN, at a frequency of 1 kHz, and an accuracy of 5 kN.

High-resolution and high-speed uplook cameras—The high-resolution and high-speed camera system specifications and performance can be found in Table 2. These cameras were co-boresighted, offset from the TV longitudinal axis by 9 degrees.

Range Instrumentation

The test vehicle included a C-band radar beacon with two, diametrically opposed antennas on the shoulder of the vehicle. The radar beacon allowed for accurate ground tracking of the vehicle during the entirety of the flight, including the expected GPS dropout.

The two radars that were used to track the test vehicle were the ROSA and the DR-COSIP.

4. Mission Operations

Launch

The launch of SFDT-2 was conducted out of the US Navy's Pacific Missile Range Facility on the West end of Kauai in the Hawaiian islands. The range provides controlled sea and air space to the West of Kauai, as well as communication and tracking assets and vehicle integration facilities. Selection of PMRF as the test site was based on reliable weather conditions near the surface for the launch of large scientific balloons as well as generally prevailing winds that take the balloon to the West in June and July, away from populated areas.

The trajectory of the balloon phase is determined by the

balloon ascent rate as a function of time and the wind direction and speed as a function of altitude. Prior to launch, the predicted trajectory must be shown to sufficiently avoid populated areas on and around the islands so that a possible balloon failure at any time during the ascent will not pose a safety hazard. In addition, the predicted balloon trajectory must permit enough time at float altitude and a set of selectable powered-flight azimuths so that the powered flight will be contained within the range boundaries for the test. These safety and operational boundaries are shown in Figure 7, where the balloon ascent must be contained in the yellow boundary.

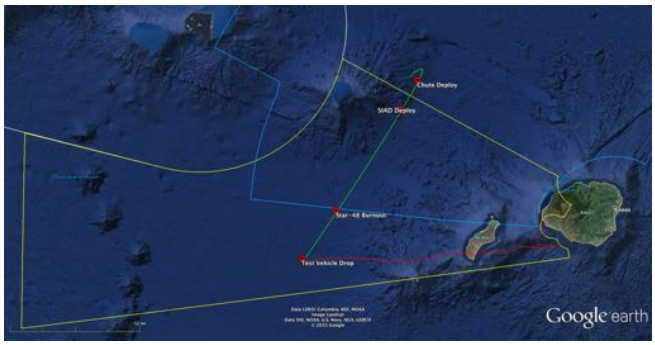

Figure 7. Balloon launch constraints and SFDT-2 Ground Track

Evaluation of a candidate launch begins the day prior to the opportunity. Using atmospheric predictions of wind, temperature, and density from NOAA's Global Forecast System, a predicted trajectory for the balloon ascent and test vehicle flight path is generated. The trajectory is evaluated against safety and operational constraints as well as favorability for science imaging due to sun location. If the constraints are met, the launch activities commence in the evening for a launch the following day.

For SFDT-2, a 10-day launch period from June 2-12, 2015 was planned with Range operations at PMRF. The first few opportunities resulted in No-Go decisions due to balloon trajectory constraint violations and unfavorable sea state conditions for recovery operations. The third opportunity, for June 4th proceeded with Go decisions but was later scrubbed due to a developing rain system moving in the direction of the launch area which could have led to unsuitable winds for balloon launch. Finally, on June 7th, suitable trajectory was forecast for the following day and launch operations commenced for a launch on June 8th.

With a targeted launch window between 7:30-9:00 am HST, the L-9 hr timeline for launch preparations had the Integration & Test team call to station at 10:00 pm HST the night before and Test Vehicle rollout from the Missile Assembly Building to the launch site started at 10:45 pm. Once at the launch site, the test vehicle was mated to the balloon gondola hardware on the launch tower. Operations of the mission were controlled by interconnected teams on the range that were at the launch site for balloon activities up to and including launch (Red Label Area), in the Range Operations Control Center (ROCC) for range systems, recovery, and overall mission direction, the Balloon Operations Center (BOC) for balloon control during ascent, and the Test-Vehicle Operations Center (TOC) for test vehicle commanding and telemetry assessment throughout the mission from pre-launch to splashdown. Figure 8 shows the locations of the facilities on the range. The range telemetry systems are on Makaha ridge.

Figure 8. PMRF Facilities

A series of checkout activities were conducted first with the test vehicle on its ground cart and later with the vehicle lifted to the launch position. The test vehicle and gondola can be seen being attached in Figure 9. The checkouts verified the operation of the test vehicle and gondola electrical systems and exercised the radio frequency interfaces with the range. At launch minus 90 minutes, the balloon inflation began and was completed around launch minus 45 minutes. At 6:25 am HAST, the test vehicle systems were powered up for launch. The umbilicals to the test vehicle were pulled at 7:04 am, and the balloon launched at 7:45 am HAST.

Figure 9. SFDT-2 Test Vehicle and balloon gondola being attached during pre-dawn operations

Ascent and Drop

The balloon ground track can be seen in red in Figure 7. The balloon trajectory initially took it off the West coast of Kauai before turning south. The balloon briefly turned East before ascending to an altitude where the winds would push it back to the West. A series of ballast drops were conducted between 8:41 am and 8:56 am in order to assure a positive ascent rate through the tropopause. At approximately 9:41 am and an altitude of 94,000 feet (28.6 km), the balloon began flying over the island of Ni'ihau and departed approximately 7 minutes later. During ascent, predictions of time at float altitude were updated though it was known that the balloon would need to spend some time at float altitude prior to reaching a suitable drop location. The balloon trajectory and pointing azimuth were updated throughout and the drop time

was selected to be 11:35 am HAST. The procedure to power up and arm the test vehicle systems for drop began at 30 minutes before drop, with all systems operating as expected.

The balloon reached its float altitude of 120,000 feet (36.6 km) at 10:21 am. At 11:33 am, the test vehicle GLN-MAC attitude was initialized as the final preparation before drop. At 11:35 am, as planned, the test vehicle was dropped from the gondola in a fully armed state using a UHF tone broadcast from the range to the Drop Receiver on the test vehicle. After the drop, the balloon was terminated and fell with the gondola to the ocean.

Flight

There was no further commanding of the test vehicle after it was released from the balloon gondola and the vehicle began a series of autonomous events. Tracking of the test vehicle was achieved by the range using an on-board C-band transponder. Real time telemetry and down-sampled situational awareness video was collected via S-band over the full duration of the flight. The ground track of the flight trajectory is the green line in Figure 7.

After release from the balloon, a timer was used to trigger two pairs of spin-up motors at 0.36 seconds and 1.67 seconds after release. The spin-motors achieved a spin rate of approximately 267 deg/sec prior to the main motor ignition at 2.18 seconds after drop. Burn-out of the main motor was evaluated as the moment that the acceleration of the vehicle went negative and occurred 72.46 seconds after drop at a Mach number of 4.17 and an altitude of 52.3 km. Shortly after burn-out and subsequent spin-down a large disturbance occurred which resulted in a momentary (less than a second) decrease in deceleration of nearly 50% and subsequently large oscillations on the test vehicle of up to 25 deg total angle of attack. To date no conclusive explanation has been found for the disturbance. Pressure transducers internal to the main motor revealed no change in internal pressure that could produce any appreciable thrust out of the Star-48. Base pressure transducers on the vehicle were near the bottom of their measurement capability but recorded no significant change during the event. Currently the primary hypothesis centers on a potential atmospheric disturbance, such as a pocket of density decrease (e.g. a pothole in the sky), though discussions with atmospheric scientists indicated that the magnitude of atmospheric disturbance necessary to produce the measured effect was unlikely.

Deployment of the SIAD-R was triggered by an algorithm that used the altitude at burnout to select a velocity at which the deployment would be triggered. This was an update from the logic used in the 2014 flight that was intended to provide robustness against uncertain atmosphere and motor performance conditions. To achieve more ideal conditions for parachute testing, a delayed SIAD deployment at a lower Mach number relative to SFDT-1 was baselined and implemented for SFDT-2. At the time of initiation of the cold-gas gg's, the vehicle was traveling at Mach 3.09 at an altitude of 52.52 km. Mortar fire of the Parachute Deployment Device occurred at 140.66 seconds from drop at a Mach number and dynamic pressure of 2.78 and 465 Pa, respectively. Line stretch of the SSRS, used as the beginning of inflation, occurred at Mach 2.37 and a dynamic pressure of 567 Pa. All of the instrumentation on the vehicle operated as planned.

After parachute deployment, the test vehicle descended to the ocean where it splashed down at 11:51 am HAST, 16 minutes after drop. An altitude (pressure) based switch on the test vehicle was used to begin an autonomous shut down of all electrical systems at an altitude of around 15,000 ft so as to safe the vehicle for recovery. Thus, the splash down time, location, and conditions are estimated from the last received telemetry prior to vehicle shutdown. The last received telemetry from the vehicle was at an altitude of 4017 m and a velocity of 30.972 m/sec. Impact velocity was estimated as 25 m/sec.

Recovery

Recovery operations for SFDT-2 began the day prior to launch with the departure of three recovery vessels from Kauai. A large cargo vessel, the 185 ft *M/V Kahana* was used as the primary vessel for recovery of the test vehicle while two smaller vessels, the *F/V Nisei* and the *Honua* were tasked with recovery of the Flight Image Recorder, in the event that it separated from the test vehicle, and balloon recovery. Two C-26 spotter aircraft were also used with one assigned for visual tracking of the balloon and one test vehicle tracking.

To aid in recovery, the test vehicle and Flight Image Recorder had Iridium transmitters periodically broadcasting their GPS based locations. Additional tracking was available via C-band transponder, until vehicle power down, and skin radar tracking, until loss of signal. The *Kahana* was the first to arrive at the test vehicle at approximately 12:45 pm HST and the *Nisei* arrived 10 minutes later. Upon arrival, it was observed that the floating test vehicle had experienced severe damage from impact but that the majority of components remained intact and that the FIR was still attached. Recovery of both items was successfully completed by 1:25 PM HST. Recovery of the parachute was completed by the *Nisei* approximately 20 minutes later. At 1:55 pm HST, both vehicles began moving towards the projected splash down point of the ballute, though the ballute would not be spotted until 3:05 PM as it appeared to have drifted/sailed several miles from the estimated location. Images of the test vehicle and ballute prior to and during recovery are shown in Figure 10.

Recovery of the balloon carcass was delayed due to complications in understanding the last known position and the search continued into the evening of the 8th. Spotter aircraft were again launched on the morning of the 9th, quickly located the balloon, and vectored the *Honua* to the location. Balloon recovery proceeded without incident from that point on.

Figure 10. SFDT-2 Test Vehicle prior to recovery (top) and ballute during recovery by the *Kahana* (bottom)

5. Atmosphere & Test Conditions

Determination of the atmosphere at altitudes of interest was achieved via a combination of Radiosonde weather balloons and Super Loki meteorological sounding rockets (MetRockets) with PWN-12a ROBINspheres. The balloons ascended to altitudes between 30 and 35 km while carrying an instrument for measuring pressure, temperature, humidity, and GPS position. The MetRockets deployed an inflatable Mylar sphere at an altitude between 80 and 90 km that was tracked via radar until collapse. Horizontal motion of the ROBINsphere was used to calculate wind magnitude and direction while the descent rate was used to derive atmospheric density. Upper atmospheric pressure is then derived from density and temperature from the combination of density and pressure. Each MetRocket measurement is anchored using the measured data from the Radiosondes at lower altitudes. For SFDT-2, four MetRockets were launched and all four inflated and were tracked until collapse with the earliest collapse occurring at 38.5 km for the third MetRocket. Reconstructed values of the atmospheric state are provided in the figures below with comparisons to both EarthGRAM and Global Forecasting System models.

The data post-processing for SFDT-2 included an Extended Kalman Filter (EKF) that combined the meteorological, IMU, GPS, and radar data. Trajectory conditions at key events were calculated from the reconstructed atmosphere and the vehicle trajectory and are summarized in Table 3. The calculation of a Mars Equivalent Altitude is based upon a Mach number scaling approach for the SFDT-2 test vehicle. That is, though the test vehicle is dimensionally matched with an expected Mars entry vehicle, the mass of the test vehicle during the test phase is approximately 1/3rd that of an expected Mars vehicle. Therefore, when applying Mach scaling approach, the Mars equivalent density is approximately 1/3rd that of the test density at Earth. Using an assumed Mars atmosphere, the equivalent Mars altitude can then be calculated.

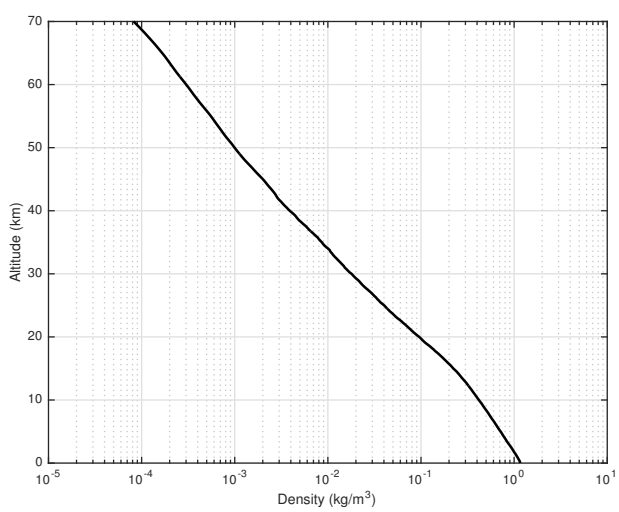

Figure 11. Reconstructed density profile.

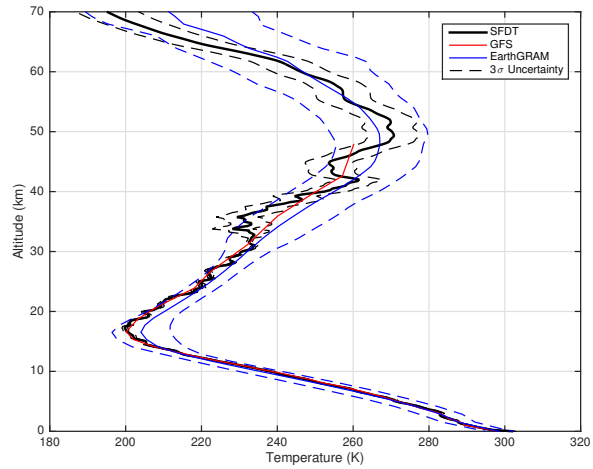

Figure 12. Reconstructed temperature profile.

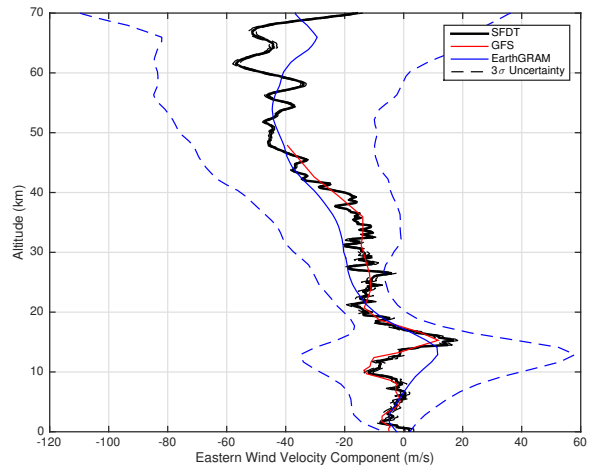

Figure 13. Reconstructed wind component in the Eastern direction.

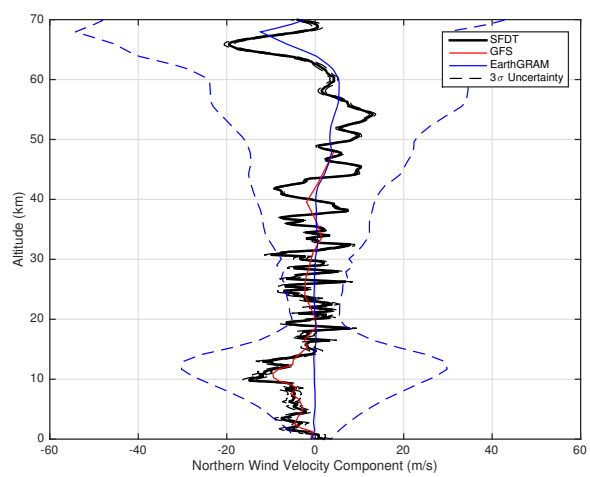

Figure 14. Reconstructed wind component in the Northern direction.

Table 3. Trajectory conditions at key test events. VT1 and VT2 correspond to the conditions at the preprogrammed Velocity Trigger points.

Event *N/A*	Time from Drop *sec*	Mach	Dynamic Pressure *Pa*	Wind-Relative Velocity *m/s*	Geodetic Altitude *km*	Mars Eq. Altitude *km MOLA*	Flight Path Angle *deg*
Drop	0.00	0.02	0.12	5.89	36.50	2.47	−2.04
Spin up 1	0.36	0.02	0.16	6.91	36.50	2.47	−31.65
Spin up 2	1.67	0.05	0.91	16.28	36.48	2.44	−70.05
Ignite	2.18	0.07	1.38	20.03	36.48	2.42	−74.83
Mach 1	26.81	1.00	225.76	314.18	39.02	4.91	46.13
Mach 2	43.61	2.00	496.79	639.55	43.54	10.40	27.28
Mach 3	58.31	3.00	624.04	985. 42	48.01	15.63	18.24
Mach 4	70.24	4.00	709.79	1317.65	51.60	18.73	12.80
Burnout	72.46	4.17	711.25	1370.80	52.24	19.23	11.94
Spin Down 1	73.52	4.13	671.99	1354.68	52.53	19.58	11.56
Spin Down 2	74.02	4.11	656.64	1349.09	52.67	19.72	11.38
VT1 Detection	126.30	3.12	359.17	1021.14	53.08	20.20	−12.85
SIAD Deploy	128.66	3.09	376.75	1013.64	52.52	19.51	−19.97
VT2 Detection	140.48	2.78	462.60	916.56	49.18	14.96	−20.16
PDD Mortar	140.66	2.78	464.61	915. 53	49.13	14.87	−20.24
Bridle Cut	150.65	2.43	545.08	783.16	45.79	9.42	−26.44
SSRS Line Stretch	152.60	2.37	567.32	757.25	45.11	8.04	−27.61
Parachute Inflation	153.212	2.24	521.12	715.63	44.89	7.67	−28.07
Mach 1.4	161.59	1.40	274.25	449.17	42.63	4.24	−33.94
Mach 1.0	171.57	1.00	191.28	319.48	40.24	0.51	−46.13
Mach 0.5	219.24	0.50	183.50	153.25	30.82	N/A	−81.17

6. SIAD-R Performance

Deployment and Inflation

Deployment and inflation of the SIAD began with the detection of the first velocity trigger, VT1, by the GLN-MAC IMU. For SFDT-2, a new triggering approach was implemented such that the target velocities at each velocity trigger were variable and dependent on the conditions at burnout of the Star-48. Based on the GLN-MAC's estimate of the altitude at burnout, the VT1 was set as 1010 m/sec. Following VT1, lens covers protecting the three SIAD situational awareness (GoPro) cameras and the high speed panoramic camera were released. Two seconds were provided for the SIAD situational awareness cameras to perform auto-exposure compensation before the next event. The SIAD Restraint and Release (R&R) covers were held down by lacing and cords that were severed with two sets of nine each pyrotechnic cutters. The second set of cutters were a redundant set in the event the first did not operate. Though the field of view was limited, no motion of the R&R covers was observed in the situational awareness cameras until the cold-gas gg's were activated and the SIAD began inflating.

SIAD inflation began with the firing of the first of two sets of gas generators. The inflation system is comprised of nine compressed cold-gas and nine combustion product hot-gas gas generators that are manifolded together. The cold-gas gg's used approximately 90 grams of gas each with a composition of mostly argon and a small amount of helium. The hot-gas generators utilized a combination of compressed $Ar/N_20/He$ and combustion products to produce about 5.2 moles of gas each. When the cold-gas gg's were fired, the SIAD emerged from a tightly packed state from behind the R&R cover and began taking shape.

For SFDT-2 a panoramic camera was not used to image the SIAD and observations of the inflation behavior rely on imagery from the two situational awareness cameras with appreciable SIAD coverage. Imagery from those cameras, shown in Figures 15 and 16, indicated a relatively uniform inflation with no large regions of the SIAD leading others during deployment. No motion of the SIAD is evident prior to the firing of the cold-gas gg's, including the R&R cover. The initial motions of the SIAD appeared predominantly in a radially outwards direction and the SIAD was not observed to wrap around the top deck. In a few images, e.g. Figure 15(c), the R&R cover can be seen providing a barrier between the SIAD and spin motor nozzles, although additional abrasion layers are present on the SIAD to prevent any damage in the event that the SIAD does make contact with nozzles. Lastly, motion of the SIAD appears to end within 10 - 20 ms after firing of the hot-gas gg's and large motions of the R&R cover end approximately 30 ms after that.

Data from the three internal pressure transducers clearly shows the initial cold gas inflation and subsequent hot gas gg firing (Figure 17). Once the cold gas generators were fired, a small pressure rise to a peak average pressure of 0.877 psia occurred, corresponding to a period where inflation outpaced the growth in SIAD volume. The rate of volume expansion quickly takes over to relieve the initial pressure rise, though subsequently a slow increase in pressure continues to occur until the hot gas gg's are fired due to the cold-gas gg's continuing to slowly deplete after the initial firing.

Firing of the hot-gas gg's quickly increases the internal pressure to approximately 4.4 psia, though some ringing is observed in the system and a peak pressure of 4.82 psia was measured by PPT3. Note that the data plotted in Figure 17 is unfiltered, so transient spikes may not represent true internal pressures. From inspection of the situational awareness imagery, observable motions of the SIAD ceased in conjunction with the firing of the hot-gas gg's and the SIAD took a visibly rigid geometry. This indicates an effective SIAD inflation time of $\sim$0.3 seconds.

Prior to the cold gas gg's firing, a small internal pressure ($\sim$0.083 psia / 572 Pa) was consistently recorded by all three transducers. This pressure is higher than the reconstructed atmospheric pressure at the altitude of SIAD deploy ($\sim$57 Pa), though it is close to the atmospheric pressure at the point of test vehicle release from the balloon ($\sim$459 Pa). Thus, the pressure recorded prior to inflation was likely a combination of some residual air remaining in the SIAD prior to inflation and not evacuating during powered flight and the rapid ascent to the test altitude, and the uncertainty in the instrumentation.

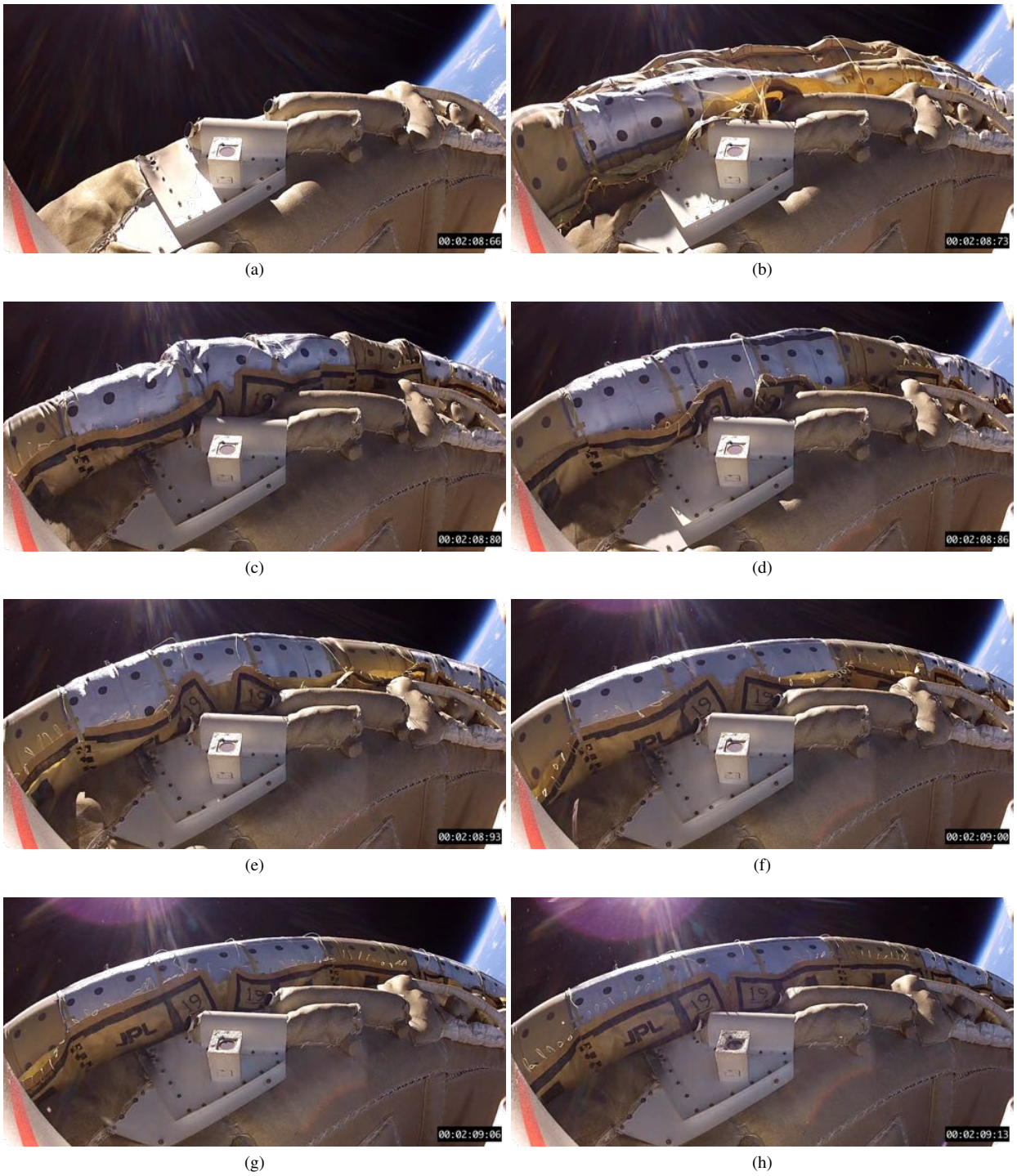

Figure 15. Initial emergence of the SIAD as viewed from a situational awareness camera looking in the region of gore 20, progressing in ∼67 ms increments. Time tags shown in each image are measured from drop and estimated to be accurate to within ∼20 ms.

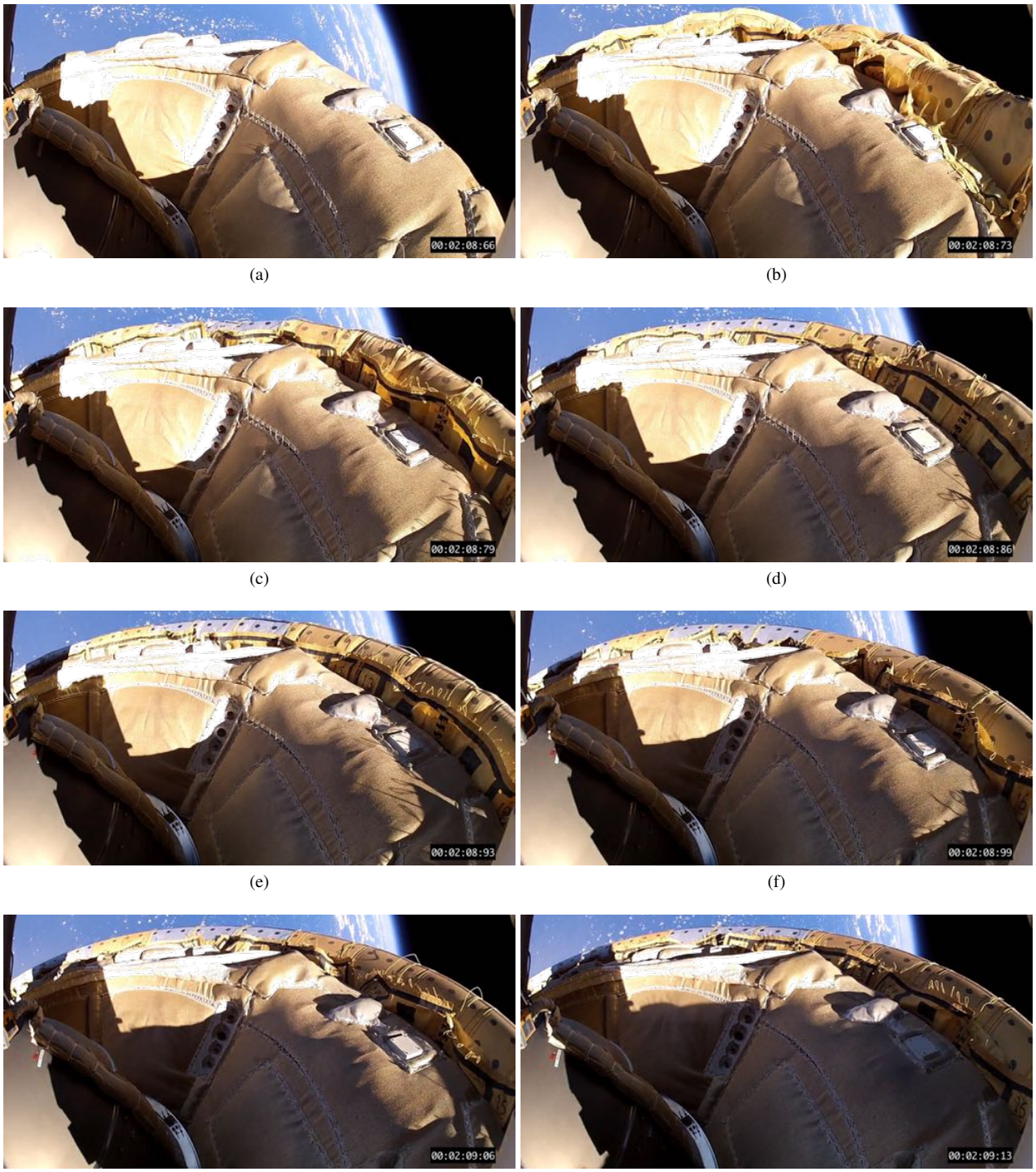

Figure 16. Initial emergence of the SIAD as viewed from a situational awareness camera looking in the region of gore 12, progressing in ∼67 ms increments. Time tags shown in each image are measured from drop and estimated to be accurate to within ∼20 ms.

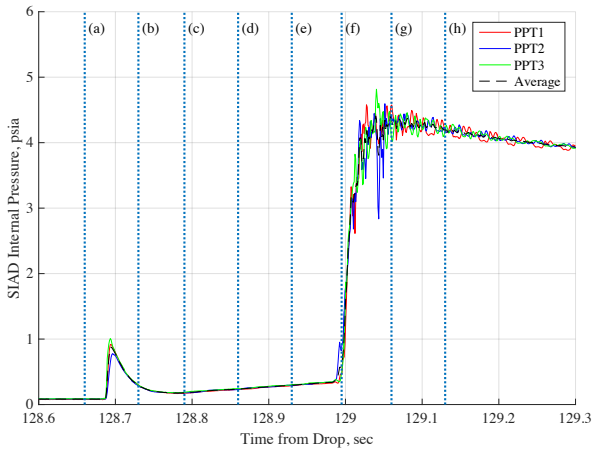

Figure 17. SIAD internal pressure history during initial moments of inflation. Vertical blue lines and associated letters correspond to subimages shown in Figures 15 and 16.

The test vehicle accelerations and rotational rates measured during the inflation event are provided in Figures 18 and 19. Overall the accelerations are indicative of a relatively uniform inflation with minor asymmetric disturbances. Axial (x-axis) accelerations indicate a transient response shortly after firing of the cold-gas gg's that is likely an indication of the emergence of the SIAD producing minor axial disturbances. These transients are seen to dampen out simultaneously with the firing of the hot-gas gg's, though some ringing remains in the raw 400 Hz measurements. Accelerations in pitch and yaw axes show smaller disturbances and only in the moments immediately preceding and after the hot-gas gg firing.

Small disturbances in the vehicle rotational rates are also evident, with rotations along the axis of symmetry of the test vehicle showing the largest relative changes. A momentary reversal in roll direction occurs shortly after the cold gas gg's fire, followed by two more direction reversals prior to the hot gas gg's firing. Though the disturbances in roll were relatively small, possible causes include internal torques being applied during inflation (e.g. one diffuser directing inflation gas in a biased direction, thus producing torque) or an initial small out of plane geometry of the SIAD prior to full pressurization by the hot-gas gg's. Rate variations in the pitch and yaw axes were seen to be significantly less than the amplitude of the already present oscillations.

Disturbances in the aerodynamic angles of attack and sideslip during inflation event were negligible. SIAD deployment was observed to increase stability of the test vehicle and reduce the magnitude of oscillations in total angle of attack while increasing the frequency of oscillation, expected behaviors with the increase in area.

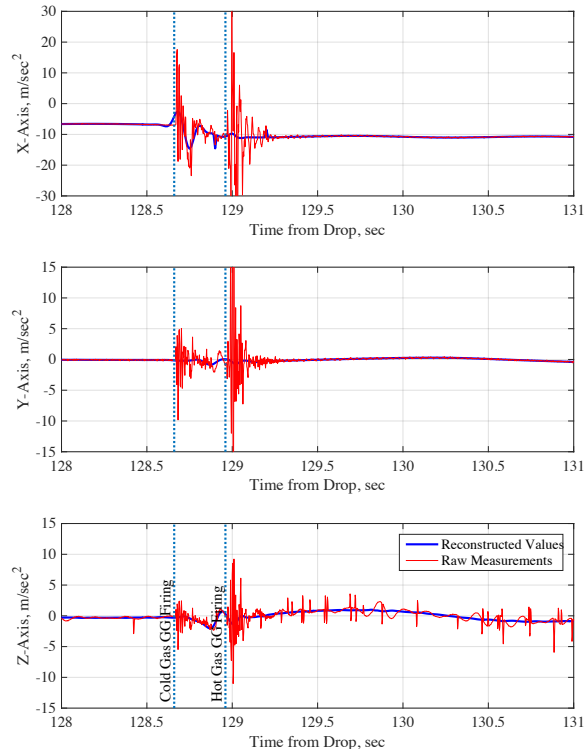

Figure 18. Reconstructed and raw measured vehicle accelerations during SIAD deployment and inflation.

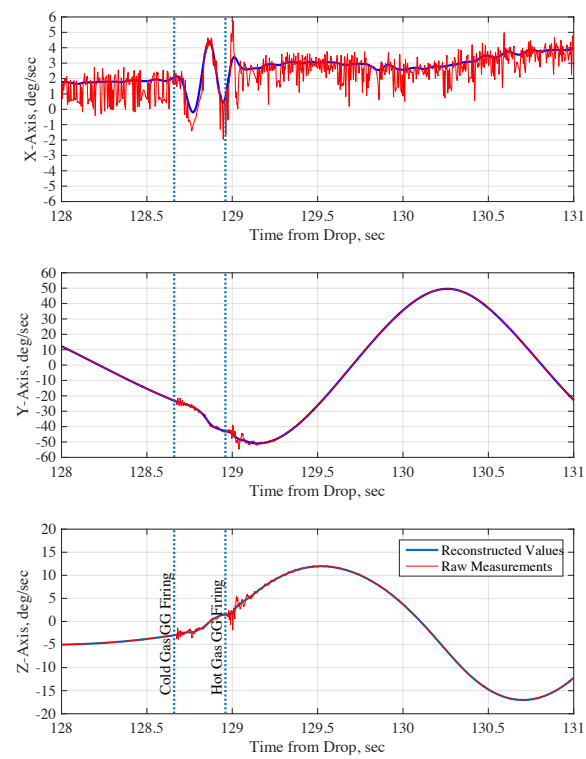

Figure 19. Reconstructed and raw measured vehicle rates during SIAD deployment and inflation.

Aeroelastic Distortion

The first flight of SFDT included an internal camera that was used to image a series of LED's installed on the wall of the SIAD. Those images were then used to correlate the axial deflection of the SIAD with changing conditions. Because of the success of the SIAD on SFDT-1 and because the objectives of SFDT-2 were focused more on the parachute, the internal camera was not used. Thus, only a less rigorous assessment of the aeroelastic performance of the SIAD-R was possible. Using the situational awareness cameras, qualitative assessments of the deflection and the occurrence of local and global deformation were possible. The situational awareness cameras also allowed for a coarse quantitative assessment of the deflection through the observation of the SIAD limb over time and during events with high dynamics. At the time of writing, this analysis is incomplete though early results do not reveal appreciable deflections during the time between hot-gas gg firing and the ballute mortar firing events, despite an increase in dynamic pressure of approximately 20% and large angles of attack during that time.

The situational awareness camera imagery was used to investigate the conditions at which the SIAD began to show the onset of wrinkling, or localized buckling of the softgoods, and at which the SIAD saw significant deformation. From the fields of view available, first signs of wrinkling occurred around 6.5 minutes after drop on the border between gores 14 and 15. Approximately fifteen seconds later, localized buckling is observable across the visible regions of the SIAD and by 7 minutes and 45 seconds after drop, the SIAD has largely collapsed. Altitudes and pressures for these events are given in Table 4. The definition and assessment of each event is somewhat arbitrary and thus the conditions should be considered approximate.

Additional comparisons of the internal and external pressures are shown in Figure 20. Around the time of first wrinkling the vehicle is on terminal descent and the dynamic pressure is negligible. However, the atmospheric pressure is building while the internal pressure is slowly decreasing until a point at which the two pressures track each other much more closely. Localized buckling of the SIAD is first observed when the difference in internal and atmospheric pressure is just over 2 kPa (0.3 psi) and global buckling is evident at a delta pressure of 766 Pa (0.1 psi).

Aerodynamics and Aerothermodynamics

The reconstructed static force and moment aerodynamic coefficients are shown in Figures 21 and 22 along with the preflight aerodatabase values associated with the vehicle state at each moment. Axial force coefficient for the vehicle was observed to be consistently larger than the preflight aerodatabase for the reconstructed vehicle state, with axial force coefficients above 1.4 for most of the SIAD flight. This trend of measured values being higher than preflight estimates is consistent throughout the aerodatabase. At the time of publication, this bias is being investigated as a potential bias in the reconstructed atmosphere. A change in density was observed in the altitudes of interest over the time period of the four MetRocket launches. Depending on the weighting scheme used with the four MetRockets, variations of a few percent are possible and would explain a majority of the observed bias.

Although the axial force coefficient decreased after SIAD inflation, a net increase in drag area ($C_D A$) of approximately 50% was achieved. Lastly the large axial force coefficients

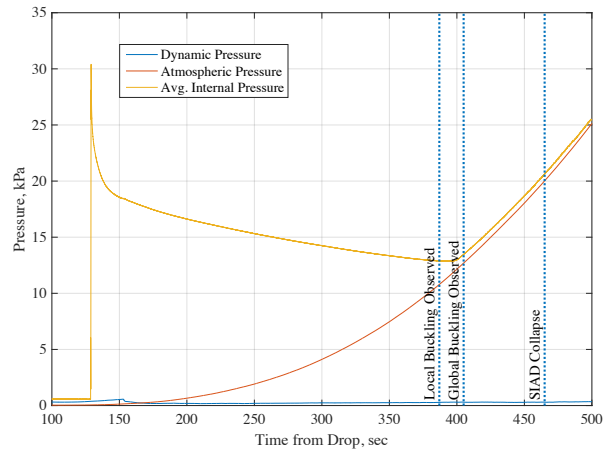

Figure 20. SIAD internal pressure, atmospheric pressure, and freestream dynamic pressure versus time with approximate times of observed SIAD deformation.

observed after PDD mortar fire in Figure 21 are artificially high as they do not account for the drag of the ballute contributing to the deceleration of the vehicle. That is, the axial force coefficient includes contributions from both the SIAD and the ballute.

Reconstructed side force coefficients show good agreement, however, the signal-to-noise ratio in vehicle accelerations in those axes is significantly lower than for axial forces and the uncertainties associated with the reconstructed values are larger. A similar situation is evident in the moment coefficients, where there is good agreement during SIAD flight between predicted and reconstructed nominals, though the reconstructed uncertainties are large percentages of the nominal value.

Close agreement in the predicted and reconstructed moment coefficients, and predictions of stability by the aerodatabase, continue to indicate static stability of the deployed SIAD-R configuration. Time histories of the wind relative angles were also indicative of a vehicle that is dynamically stable down to Mach numbers of 3.0 or lower.

The SIAD was instrumented with a number of externally and internally mounted thermocouples (TCs) to track inflation gas temperatures and assess the aerothermal environment encountered. The time history of internal gas temperatures is provided in Figure 23. Overall the thermocouples show good agreement throughout the flight with the exception of an offset prior to SIAD inflation. The offset was not unexpected given variances in packing and a near certitude in differing degrees of insulation afforded by the SIAD at different locations.

The initial spike in temperature around SIAD deploy corresponds with the hot gas generator combustion products, which begin cooling off immediately after the SIAD begins expanding in volume. Preflight estimates of hot-GG exhaust temperatures were approximately 375 °C, significantly higher than the observed peak. However, the response rate of the TCs is such that they would not be capable of measuring a fast-rising transient peak in temperature.

Table 4. Approximate conditions for the onset of localized buckling, global buckling, and large scale SIAD collapse.

Condition	Drop+ Time, min:sec	Altitude, km	Atm. Pressure, kPa	Int. Pressure, kPa	Dyn. Pressure, Pa
Local Buckling	6:27	16.154	10.789	12.888	281.8
Global Buckling	6:45	15.188	12.697	13.463	299.1
SIAD Collapse	7:45	12.384	20.025	20.630	299.0

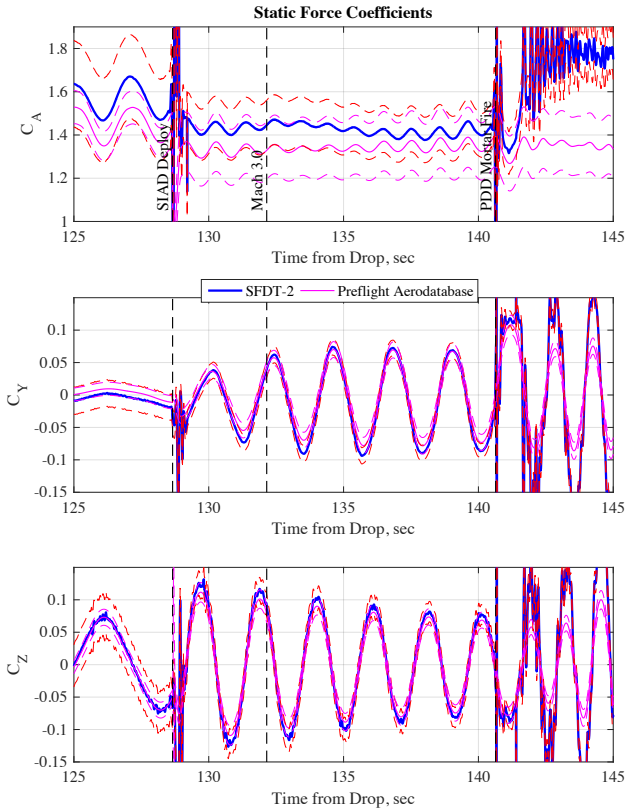

Figure 21. Reconstructed and preflight aerodatabase static force coefficients during SIAD flight. Dashed red lines correspond to the 3σ uncertainty values from reconstruction.

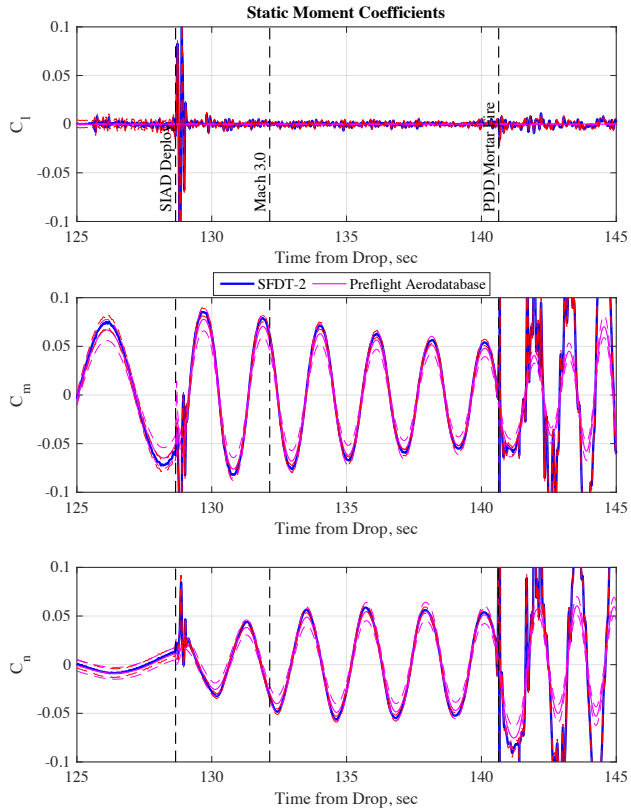

Figure 22. Reconstructed and preflight aerodatabase static moment coefficients during SIAD flight. Dashed red lines correspond to the 3σ uncertainty values from reconstruction.

Time histories of the external TC measurements are provided in Figures 24, 25, and 26. Overall, surface temperatures were seen to be benign, with peak temperatures of about 80 °C. The low temperatures were likely influenced by a delayed SIAD deployment at a Mach number of 3.08, versus the design Mach number of 4.0 or above. Temperatures at specific TC locations are seen to be relatively consistent for each of the three radial locations. Furthermore, the temperatures indicate a local grouping. For example, TC-2 and TC-5 consistently report the highest temperatures while TC's -1, -4, and -6 all report similar temperatures and TC-7 reports the lowest temperature. The result of peak temperatures occurring at the TC-2 and TC-5 locations is consistent with preflight aerothermal analyses of the deployed SIAD-R configuration. Those analyses indicated large separation regions at the SIAD and TV interface and immediately in front of the burble fence with shear layer impingement, and increased convective heating, in the neighborhood of TC-2 and TC-5. The low temperatures from TC-7 are due to its location on the backside of the SIAD. No measurements for TC-3 on Radial B are provided as that TC was observed to be damaged during installation and non-functioning prior to flight.

Peak temperatures for all thermocouples occurred at roughly the same time, between Mach 2.0 and 1.5. Although this was later than the peak heat rate estimates, the difference in time points to a degree of lag in the thermal response of the SIAD material. Given the areal density of the coated Kevlar, along with increased thermal mass associated with TC installation, this was not unexpected.

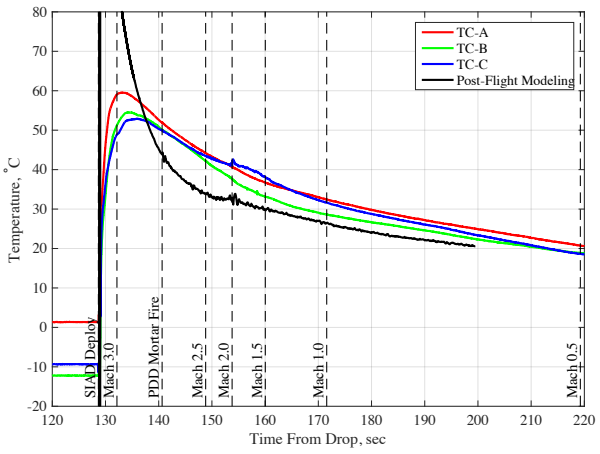

Figure 23. Time history of internal SIAD gas temperatures.

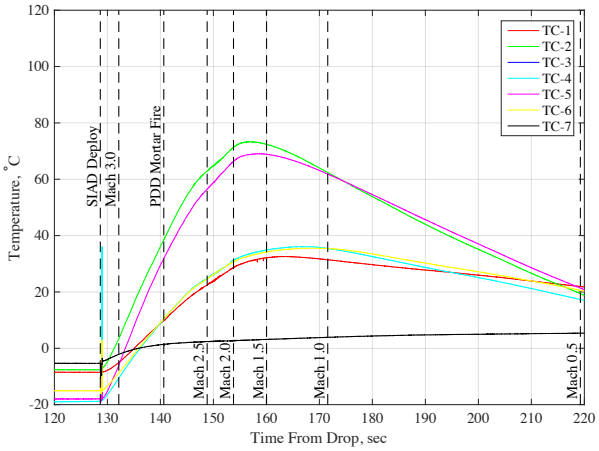

Figure 25. Time history of measured SIAD temperatures along Thermocouple Radial B.

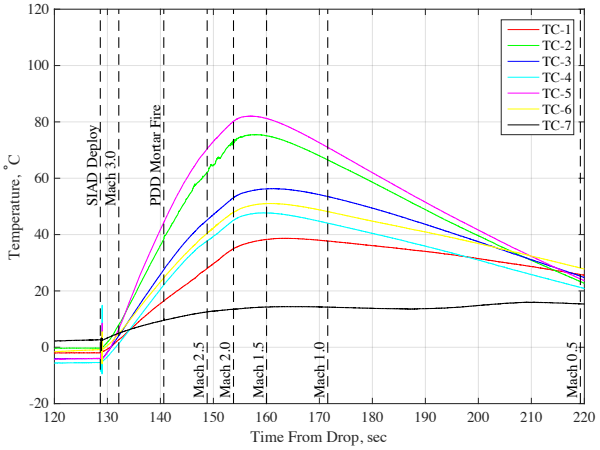

Figure 24. Time history of measured SIAD temperatures along Thermocouple Radial A.

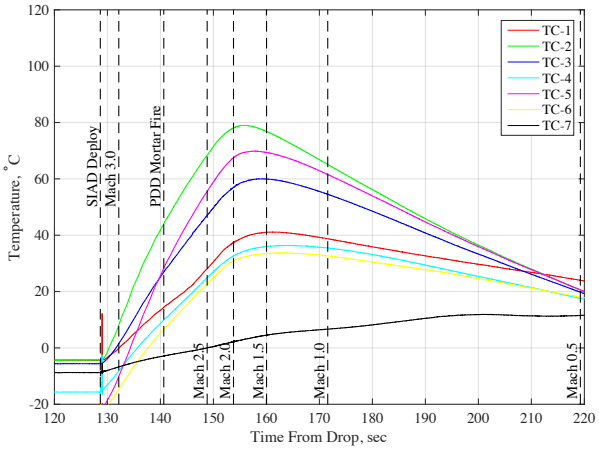

Figure 26. Time history of measured SIAD temperatures along Thermocouple Radial C.

Post-Test Observations

After recovery, the SIAD was removed and shipped back to the manufacturer for a detailed, post-flight inspection. As with SFDT-1, inspection is complicated by the manner in which the SIAD is recovered and damage that occurs during recovery and handling. Although the inspection report lists several instances of damage, the performance of the SIAD during flight would indicate that all of this occurred after the primary SIAD test phase, e.g. during descent through the lower atmosphere, impact with the water, recovery, or subsequent handling and removal from the test vehicle. A possible exception was damage observed to the diffuser assemblies which may have occurred during gg firing.

7. Parachute Deployment Device Performance

The Parachute Deployment Device (ballute) was initially considered a test artifact of the LDSD technology development as it was a device required for parachute deployment on SFDT but not something that was originally envisioned as being a technology delivery. However, the success of the PDD on SFDT-1 led to the consideration of the ballute as a viable decelerator technology, not just for parachute deployment but for high Mach, trailing decelerator applications as well [5]. Although the focus of SFDT-2 was on achieving a good test of the parachute, some additional consideration to acquiring more data on ballute performance was also applied. Specifically, the time between ballute mortar fire and the initiation of parachute deployment was extended from five seconds during SFDT-1 to ten seconds during SFDT-2. This allowed for additional drag and dynamics data to be gathered as well as additional imaging of the ballute during supersonic flight.

Deployment of the PDD was initiated by detection of the second velocity trigger (VT2) by the GLN-MAC IMU. The deployment consisted of firing four non-redundant pyrotechnic cutters used to secure the PDD triple bridle to the top deck of the Test Vehicle as well as simultaneously initiating/firing the PDD mortar gas generator at 140.66 seconds after Test Vehicle drop. From on-board acceleration measurements and high-speed imagery the mortar muzzle velocity was estimated as 60.0 m/s, consistent with ground based test results of 57 - 61 m/s. An image of the initial emergence of the ballute pack into the High Resolution camera field of view is shown in Figure 27. The debris seen in the image is associated with alumina mat insulation on the triple bridles and vehicle top deck and was expected. Line stretch of the ballute pack was assessed using the high-speed imagery and the line stretch velocity was estimated as 45.4 m/s. Prior to line stretch, a considerable amount of line sail was evident and likely influenced by vehicle dynamics prior to and during ballute deployment. Specifically, residual oscillations from the post-spin down disturbance were present and likely contributed to the large transverse motion evident in the riser. Because of these waves, by the time line stretch occurred the ballute had already begun emerging from its bag.

A time history of the loads in the ballute bridles is provided in Figure 28. The peak force of 3413 lbf at 141.73 seconds is coincident with line stretch and the snatch force associated with arresting the motion of the ballute and inflation aid. After line stretch a significant amount of rebound of the ballute was evident as the ballute continuing inflating. The multiple spikes in ballute force shown in Figure 28 are associated with those recoils and subsequent snatch events

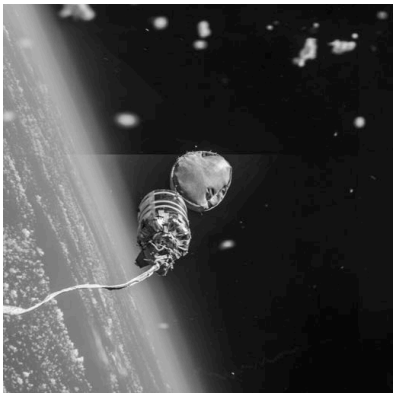

Figure 27. Emergence of the ballute pack and mortar cover off the back of the test vehicle.

and are seen to damp out considerably after the first few occurrences. Also of note is the spike in force prior to line stretch, at 140.82 seconds. The ballute pack included a riser restraint tie that was intended to ensure that the ballute did not begin deploying until the triple bridle had been stood up. The strength of this break tie is such that it produces a large snatch force coincident with triple bridle stand up.

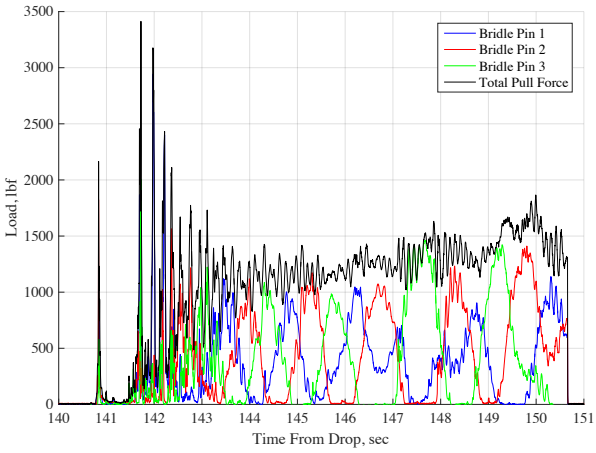

Figure 28. Ballute load history from mortar fire to triple bridle cut.

Inflation of the ballute is facilitated by an inflation aid containing an aqueous water/alcohol mixture that vaporizes when released into the ballute. This inflation aid is triggered via a pair of redundant lanyards that are attached to the leading edge of the ballute's burble fence. When the burble fence emerges from the ballute pack, the lanyards become taught and activate pyrotechnic initiators on the inflation aid. The ballute inflation sequence is shown with cropped images from one of the High Speed cameras in Figure 29 beginning shortly after the inflation aid is estimated to have been triggered and proceeding up to the point of full inflation.

Post-test estimates of the inflation aid performance calculated that the inflation aid would provided approximately 70% of the total inflation pressure based on the conditions at deployment and line stretch. The full geometry achieved by

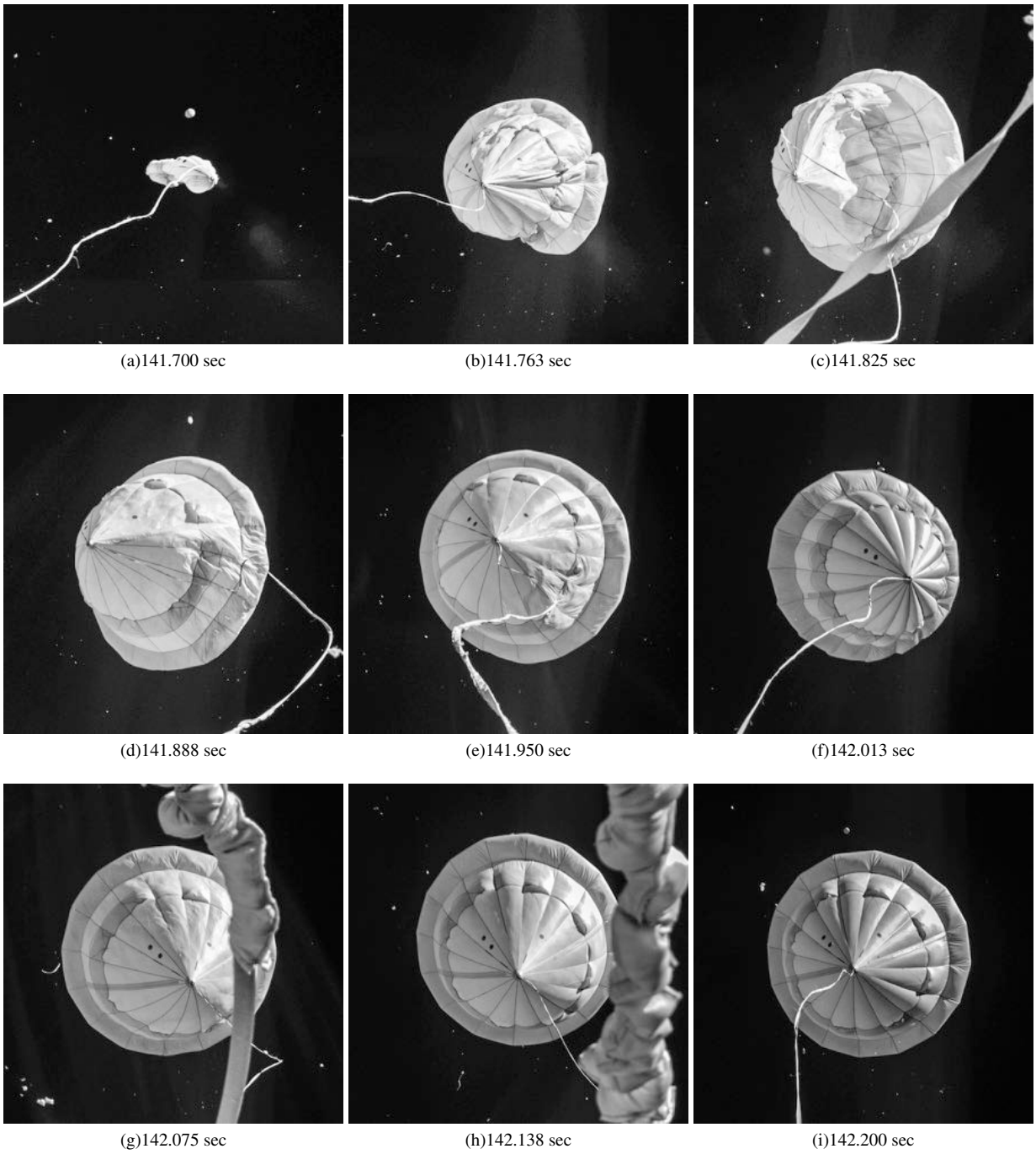

(a)141.700 sec (b)141.763 sec (c)141.825 sec

(d)141.888 sec (e)141.950 sec (f)142.013 sec

(g)142.075 sec (h)142.138 sec (i)142.200 sec

Figure 29. Ballute line stretch and inflation sequence. Times are after drop time.

the ballute is indicative (see Figure 30) that the ram-air inlets performed well enough to provide the remaining pressure required and to maintain the internal pressure throughout ballute operation. Early on in the inflation both the raised and flush ram-air inlets can be seen to be open and ingesting air while in later images the flush inlets are closed while all raised inlets show good fullness. The inflation time from activation of the inflation aid to full inflation is estimated to have taken between 1/3 and 1/2 of a second.

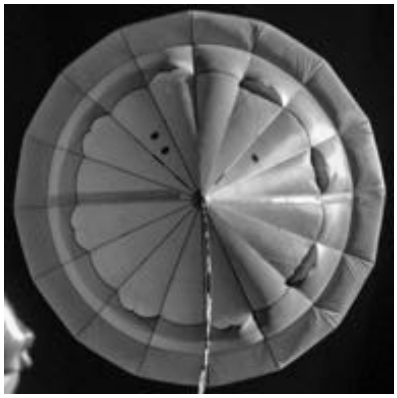

Figure 30. The ballute at full inflation with open and stable inlets.

Based on the uplook cameras, the ballute appeared to exhibit large dynamic motions. However, the imagery is confounded by the dynamic motion of the test vehicle during this portion of flight. To facilitate the reconstruction of the ballute performance, an engineering model of the inflated ballute was used with photogrammetry techniques to back out the position and attitude of the ballute relative to the test vehicle. This assessment indicated that the ballute would generally follow the motions of the test vehicle and in particular tended to follow a projected wake from the test vehicle. From the photogrammetry, an estimate of the ballute total angle of attack, defined as the angle between the ballute pull vector and the relative wind vector, was made and the results are shown in Figure 31. Times where there is no data are when the ballute had exited the cameras' fields of view. The ballute total angle of attack generally remained at 3 deg or lower and peaked just above 5 deg towards later portions of flight, implying the aerodynamic stability of the ballute was quite good for a trailing supersonic decelerator.

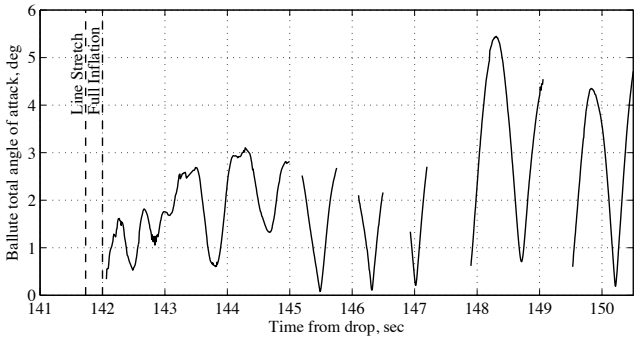

Figure 31. Reconstructed ballute total angle of attack.

The ballute load pin data was used to calculate a ballute total force coefficient and drag coefficient, where the former is the force acting on along the pull direction of the ballute and the latter is the force in the wind-relative direction. This data, as a function of Mach number, is shown in Figure 32. Both sets of force coefficients are seen to average between 0.6 and 0.8 during most of the ballute flight with a peak of just over 1.0 occurring later. Furthermore, there is a trend of increasing force coefficient with decreasing Mach number, a common trait of trailing supersonic decelerators that exist in the dynamic pressure deficit of a blunt body's wake.

Also shown in Figure 32 is a comparison against the pre-flight aerodynamic model developed for the ballute. Following the higher than expected ballute drag performance during SFDT-1, a new drag model was developed that accounted for the ballute's position in the wake of the test vehicle. Applying this model to the calculated ballute position shows general agreement in the trend of ballute drag force but that the measured forces were still biased to be higher than anticipated by roughly 10%. Part of the bias may be attributable to the density bias in the reconstructed atmosphere that was mentioned earlier, though it is unlikely to be of that large of a magnitude. Additional contributions may come from the larger vehicle angles of attack seen during SFDT-2 as compared to those that were present in the preflight ballute aerodatabase CFD cases, particularly at lower Mach numbers where the angles of attack peaked above 30 deg.

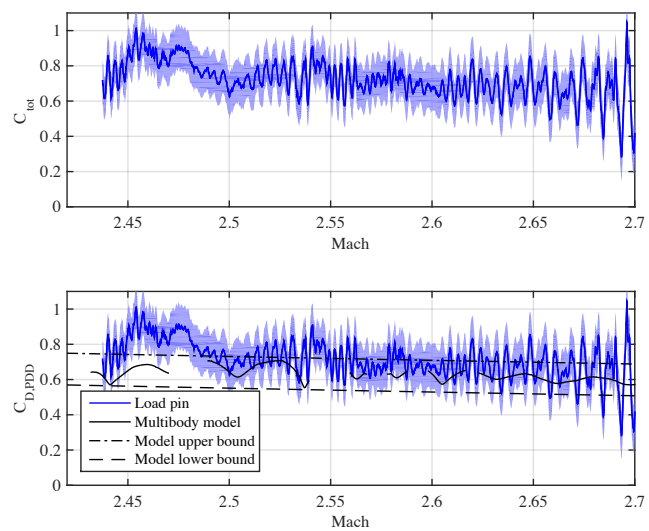

Figure 32. Ballute total force coefficient, C_{tot}, and drag coefficient, C_D, reconstructed from unfiltered load pin measurements as a function of wind-relative Mach number. Lighter shaded regions indicate the 3σ confidence intervals.

An inspection of the ballute occurred after recovery by personnel from JPL and the Naval Air Warfare Center at China Lake. The inspection revealed that the inside and outside of the ballute were almost entirely undamaged, although the lower, windward portions of the ballute and burble fence were covered in small black spots, ranging in size from less than 1/16 inch to approximately 1/8 inch which appeared to be debris from the Star-48 motor after burnout. A few light colored patches on the ballute were also seen on the windward side of the ballute, though it is not known if those existed prior to or after packing of the ballute.

8. Supersonic Ringsail Parachute Performance

Deployment of the parachute began with the cutting of each leg of the PDD triple bridle by a set of cutters triggered by a timer for 10 seconds after PDD mortar fire. After triple bridle cut, the ballute load is transferred to a lazy leg attached to the parachute pack and at this point the PDD began pulling the parachute pack off the back of the Test Vehicle. The parachute triple bridle was deployed up off the top deck of the vehicle and a series of internal carbon rods were used to help support the positioning the triple bridle until adequate tension could be established in the load train. Following bridle stand up, the suspension lines were observed to deploy cleanly from the parachute pack without any tangling or dumping. For the SFDT parachute deployment architecture, the parachute pack utilizes a unique design where at a prescribed distance the outer portion of the parachute pack separates from an inner bag containing the canopy and some length of suspension lines. The ballute and outer bag then continue aftwards, fully separated from the inner bag and test vehicle. Imagery and reconstruction of the ballute position and velocity versus time indicated that this occurred cleanly.

The parachute pack achieved line stretch 1.95 seconds after PDD bridle cut and 152.60 seconds from Test Vehicle drop. Prior to line stretch, the suspension lines appeared orderly with only a small degree of line sail evident. Initial emergence of the parachute also appeared orderly. Based upon the load cell data and high speed imagery it is estimated that bag strip occurred between 0.17 and 0.23 seconds after line stretch, with the latter time being when the parachute vent is first visible in the high speed imagery. A concern going in to the SFDT campaign was a race condition between parachute deployment from the bag and parachute inflation, where a greater potential for parachute damage exists if appreciable parachute inflation occurs with the bag still attached. From the SFDT-2 imagery set, very little inflation was evident during the estimated period line stretch and bag strip.

Parachute inflation, from the time of line stretch to peak load, occurred over 0.60 seconds. The time trace of parachute loads during and past inflation are provided in Figure 33 and an image sequence of inflation from one of the uplook situational awareness cameras is shown in Figure 34. The initial inflation was observed to occur in a significantly more orderly manner than on SFDT-1, and in general very orderly for a supersonic parachute inflation in a low-density environment. Following SFDT-1, two major changes to the parachute packing procedure were incorporated. The first included a modification to how the lines were packed and the second was to move from a z-fold style long fold to an accordion fold. The latter was intended to provide a more uniform inflation of the parachute absent large asymmetries and from the imagery of SFDT-2, this appears to have been successful. The inflation was largely symmetric, particularly in the later phases of inflation, and no entanglement of the canopy was observable. However, at or near the moment of full inflation, the parachute began to develop catastrophic damage which subsequently led to the development of a large radial tear and later, complete failure of the canopy. A close examination of the timing of critical damage observed in the high speed imagery showed that the large radial tear eventually led to the failure of the canopy skirt band 12 ms after full inflation. The parachute geometry subsequently went through large oscillations though still retained a largely inflated shape until the vent band also failed, 0.649 seconds after full inflation and 153.861 seconds after drop.

Parachute forces measured during inflation were within expectations for the conditions, e.g. Mach and dynamic pressure, at parachute deployment. A snatch force of 10,060 lbf was measured just after the moment of line stretch and an overall peak force of 79,400 lbf was measured at full inflation of the parachute. After full inflation the measured parachute force drops off precipitously but rebounds to nearly 60,000 lbf even though the parachute skirt band had failed by that time and the parachute was no longer a closed structure.

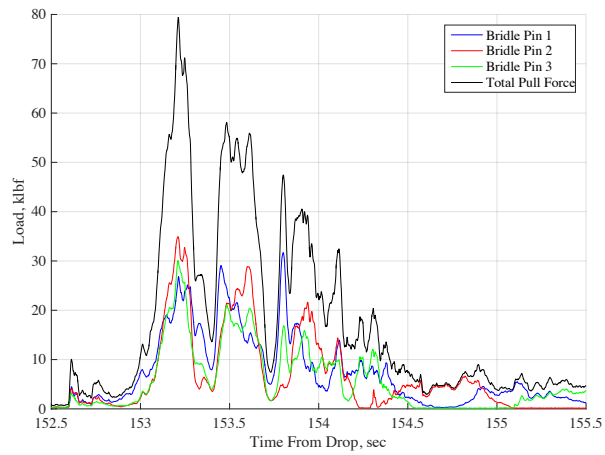

Figure 33. Parachute bridle and total forces measured during inflation.

A mapping of all damage observable in the canopy is provided in Figure 35. Multiple instances of damage were observable prior to full inflation but these were not believed to be related to the primary failure. In particular, for the regions denoted "A" and "B" in Figure 35 the damage was visible from the first moments that those regions came in to the field of view of the cameras. The damage in region "A" is a panel that tore loose from the radial main seam and though not visible in Figure 35, it can still be seen attached to the opposite radial main seam in later images. The damage in region "B" is of a similar nature where the panel has begun to break loose from the radial main seam on both sides but sill remains attached at the corners. Neither of those two damage locations can be seen to propagate any further until significant damage has already occurred to the rest of the parachute. Because the damage appears early on it is thought to have been associated with deployment and unfurling of the parachute, where those two regions may have had a small entanglement as they emerged from the bag.

Parachute damage in the "C," "D,", and "E" regions appears to be the locus of what ultimately led to the parachute's failure. The damage in that region is a combination of damage that is present very early on and damage that appears later as that region of the parachute becomes more highly stressed. A more detailed progression of the damage propagation in the area is provided in the sequence of Figure 36. Note that duration of time from the first image of Figure 36 to the last is 104 ms. The first appearance of damage in that region is a small pinhole that appears in the 12th panel of gore 40 (panel 10 is a panel immediately adjacent to the gap) that is faintly visible in 36(a) but more visible in 36(c). From high resolution imagery (not shown here), the pinhole is estimated to be on the order of a few centimeters in size and is present

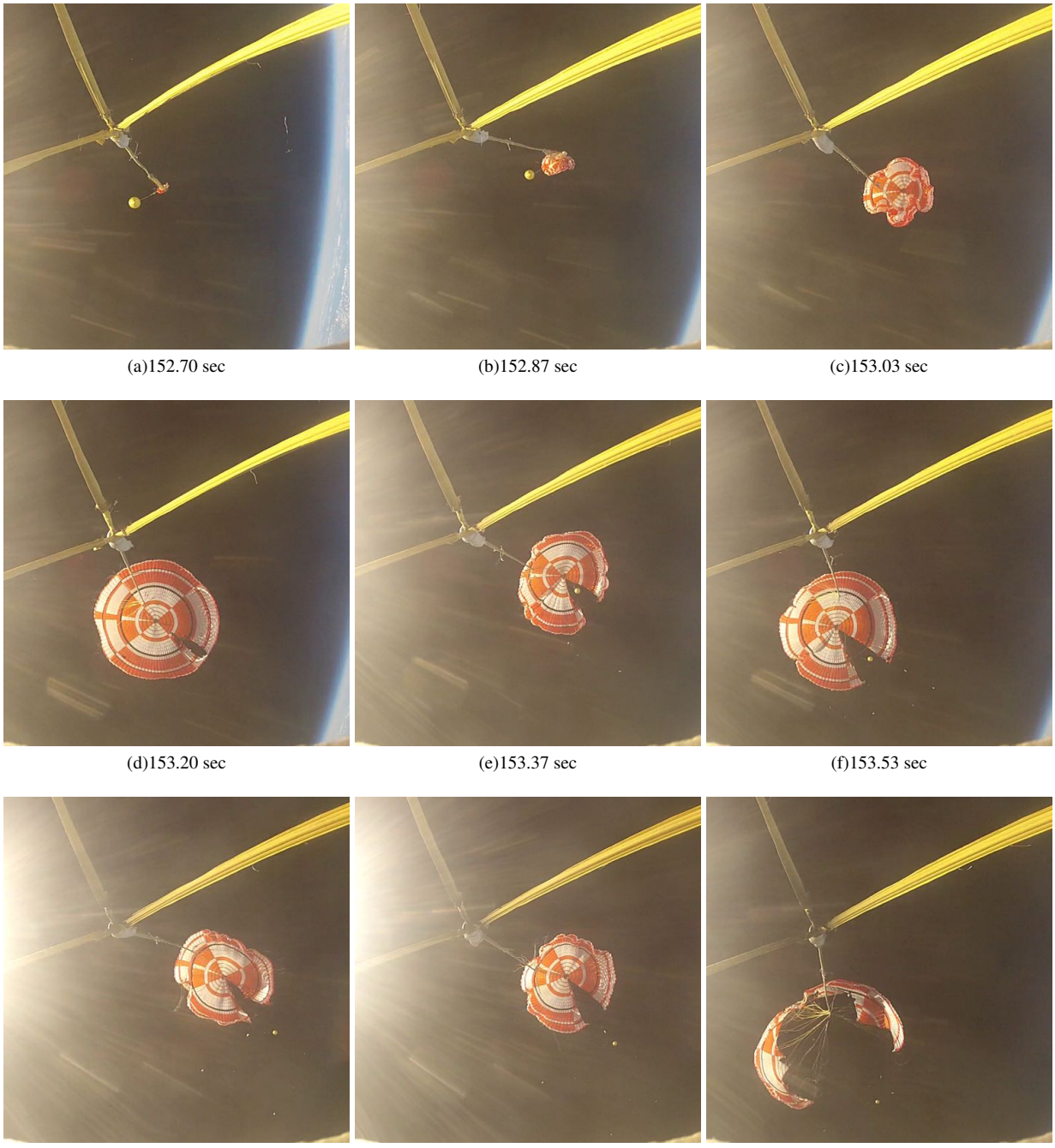

(a)152.70 sec (b)152.87 sec (c)153.03 sec

(d)153.20 sec (e)153.37 sec (f)153.53 sec

(g)153.70 sec (h)153.87 sec (i)154.03 sec

Figure 34. Parachute inflation sequence from a situational awareness camera. Times shown are from drop +/- 33ms.

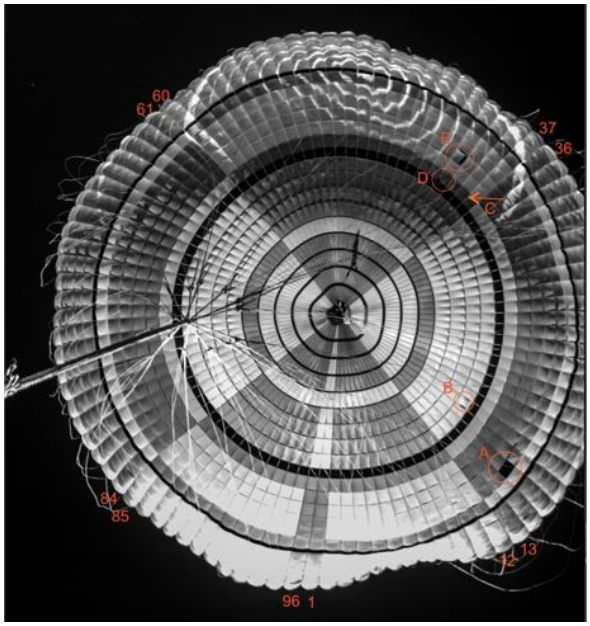

Figure 35. Map and annotations of parachute damage. Gore numbers are labeled outside of canopy.

from the first moment that the panel is visible. The pin hole remains small for several frames but begins growing towards a corner in Frame 36(e), indicating that the canopy is beginning to become more stressed in this region. The first sign of damage in region "C" also appears in Frame 36(e) as a tear along the main seam of panel 10 on Gore 38. The tear in panel 12 ultimately propagates to the point of nearly separating the panel. The critical failure appears in Panel 36(h) on the trailing edge corner of panel 10 on gore 40. In that image, the Kevlar circumferential on the trailing edge of panel 10 has failed on the corner, thus removing one of the key structural elements of the canopy. The main seam separation on that same panel further indicates a region of very high circumferential stresses. In the next frame, 36(i), the circumferential on the trailing edge of panel 11 has also failed and panel 11 has broken free. The failure of circumferentials continues in both directions, across the gap and also towards the skirt band, largely along a single radial. Of note is that the skirt band failed as soon as the unzipping action arrived at the leading edge of the canopy. However, the vent band held for approximately three-quarters of a second further before also breaking. After that moment, the parachute splits down several more radials and proceeds to lose numerous panels.

The failure of the Ringsail parachute on SFDT-2 was a surprise in both the load at which it failed at, less than 80,000 lbf, and the location of what appeared to be the critical failure, the circumferential skeletal element at the trailing edge of panel 10. That circumferential, and the next two circumferentials to fail were 800 lbf Kevlar tapes with an as-tested strength closer to 1000 lbf. Although the design load of the parachute was 80,000 lbf with a 1.5 factor of safety, the margins that were thought to exist on the circumferentials were quite large and the analyses used in the design of the parachute pointed to an overall parachute capability closer to three to four times the 80,000 lbf design load. Furthermore, the parachute design had been structurally tested as part of LDSD's Parachute Design Verification test architecture [6]. During that test, the canopy was taken to a load of approximately 120,000 lbf without encountering damage.

In the weeks and months following the SFDT-2 test, the LDSD project convened multiple reviews of the parachute design, design analyses, and the SFDT-2 test data with parachute experts from across the nation. To date, no conclusive reason or set of reasons has been identified that can fully explain the failure of the Ringsail parachute. Following the first of the reviews, the investigation into the failure focused on two primary areas: either the loads were significantly higher than were calculated by the stress analyses or that the strength of the circumferentials was significantly lower than what was seen during static testing of the circumferential joints. Both of these possibilities are discussed below. Although several other possible mechanisms were presented as possibilities, for example workmanship, many of those were not easily testable or otherwise provable, and thus were not the focus of follow-on efforts.

Significantly Higher Stresses Than Predicted: Stress analyses conducted in support of the LDSD Ringsail design took the form of analyzing a fully-inflated parachute geometry with a uniform pressure distribution and increasing the internal pressure until a prescribed total load is achieved. Stresses and loads internal to the parachute canopy originate from two primary sources, pressure vessel stresses that take the form of the product of a local radius of curvature and a pressure differential, and forces associated with the local acceleration or deceleration, often termed "inertial" or "snatch" forces. With regards to the former, large asymmetries in pressure distribution can contribute to geometries and local pressures that differ from those that were used in the analyses. Factors used in the quasi-static analyses attempted to cover the degree of asymmetry and dynamics in the parachute inflation. In particular, the internal pressure was increased to arrive at a total load of approximately 167,000 lbf, at which point margins were required to be positive with a 1.5 factor of safety and additional knockdowns, e.g. seam and joint efficiencies, applied. In the months following SFDT-2, several additional quasi-static analyses were conducted that attempted to create a variety of asymmetric geometries with asymmetric pressure distributions. The results of those analyses have yet to generate augmentations significant enough to explain the circumferential failure.

The inflation of the SFDT-2 parachute was faster than predicted and likely the fastest inflation of a large supersonic parachute ever in terms of diameter to inflation time. Because of this, a number of attempts were made to quantify the snatch forces that exist in the region of the canopy that failed. These took the form of using estimates of the velocities of the circumferentials prior to the time of failure and the mass associated with those elements and calculating a snatch force based on Hooke's law and known strengths and elasticities of the Kevlar circumferential tapes. These calculations estimated that snatch forces could have been approximately 20% of the material strength of the Kevlar circumferential, which even in conjunction with other stress analyses were not sufficient to break the circumferentials.

Material Strengths Lower Than From Testing: Two primary mechanisms of potential differences in the strength of the circumferential were focused on following SFDT-2, strength loss due to temperature and high strain rate effects. Prior testing of Kevlar had indicated that it retains roughly 50% of its strength at temperatures around 300°C. Estimates of temperatures based on the conditions at deployment, the

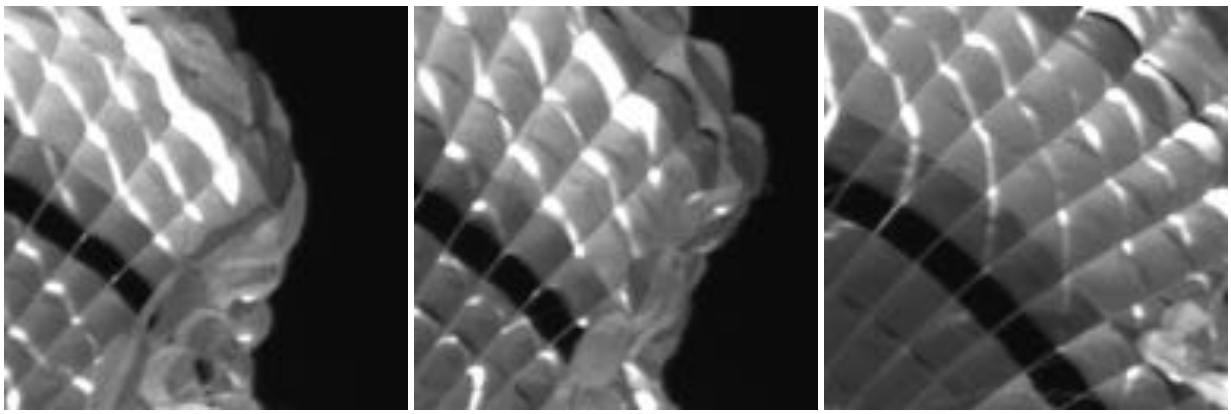

(a)153.092 sec (b)153.107 sec (c)153.129 sec

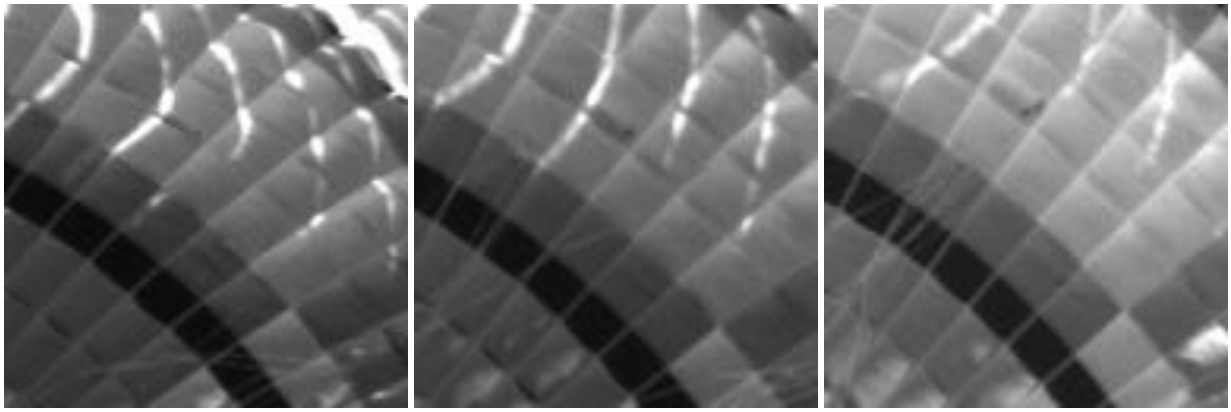

(d)153.144 sec (e)153.170 sec (f)153.184 sec

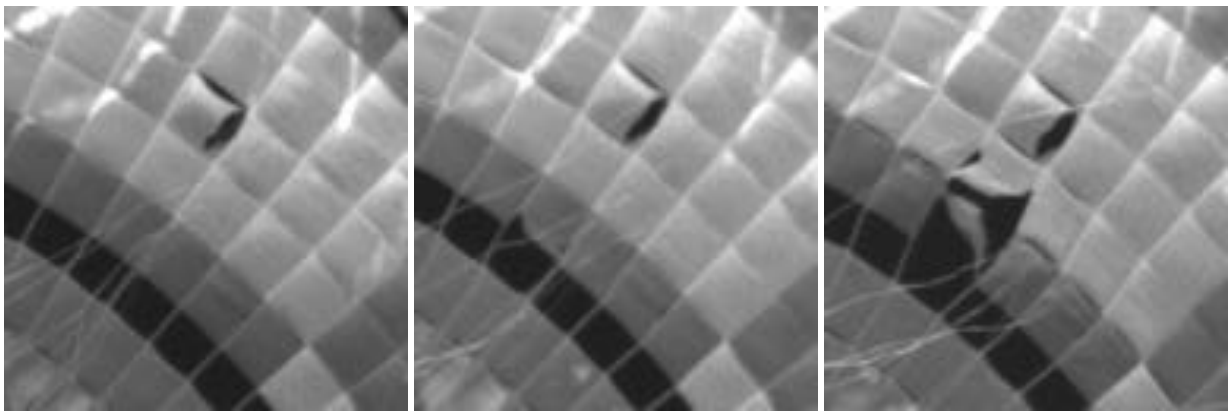

(g)153.188 sec (h)153.192 sec (i)153.196 sec

Figure 36. Progression of damage at gore 38, panel 10; gore 40, panel 12; and gore 40, panel 10 trailing edge. Times shown are from drop.

speed of the inflation, and the thermal mass associated with the Kevlar circumferential, indicated that achieving even those temperatures is unlikely.

Previous work has indicated that Kevlar may be susceptible to strain-rate in its breaking strength (e.g. Reference [7]). LDSD conducted a number of tests on Kevlar joints of the type that failed during SFDT-2. These tests included uni-axial high speed snatch tests and bi-axial tests where a radial element would be preloaded prior to a circumferential element being snatched. These tests were intended to be relatively simple screening tests to see if more intricate testing was warranted. However, they have not produced large deviations in breaking strengths of the Kevlar joints at strain rates of those estimated for SFDT-2.

Although analyses and testing conducted to date have not been able to generate loads capable of failing the Kevlar circumferential, it is felt that the analyses and tests conducted prior to SFDT-2 were inadequate for the Supersonic Ringsail configuration.

9. Summary

The SFDT-2 flight experiment met all of the minimum success criteria, as well as two of the three full success criteria. The devices were all deployed into the proper conditions, all of the planned data was acquired, and all of the hardware articles were recovered. Both the SIAD-R and ballute demonstrated excellent performance in deployment, drag, and stability. In addition to the SIAD-R, the ballute has become a delivered technology from LDSD and is being considered for potential future Mars missions.

The Ringsail parachute on SFDT-2 failed at full-inflation. One of the three full success criteria, maintaining parachute integrity for three minutes, was not met. Considering the rigorous subsonic testing the parachute design was subjected to and passed, preceding the SFDT-2 flight, the failure seen supersonically has forced reevaluation of the approaches used for qualifying supersonic parachutes for Mars missions. All of the strength tests of the parachutes for Mars Pathfinder, Mars Exploration Rover, Phoenix, and Mars Science Laboratory were done subsonically using low-altitude drop tests and wind tunnel tests. The same approach was used for the SFDT-2 parachute, where that design survived a 120,000 lbf load, presented subsonically. However the same parachute design failed in SFDT-2 supersonically at a load of approximately 80,000 lbf. It is not yet known if or how this impacts planned future applications of disk-gap-band parachutes at Mars, which are of a different configuration than the Ringsail tested on SFDT-2, and which would be expected to have different failure modes in the canopy.

In this sense, it was fortunate to have experienced the parachute failure in SFDT-2. SFDT was never intended to be a loads test. The presented load of 80,000 lbf was at the very high end, around the 98th percentile, of the expected load cases for this flight, and was a consequence of an unexpected (and unexplained) disturbance on the vehicle shortly after spin-down. Had the load at inflation been closer to the targeted mean of 58,000 lbf, well below the design flight limit load, it is quite possible that the parachute would have survived in SFDT-2, and the potential vulnerability in the historical Mars parachute strength qualification approach would not be known.

Overall, the SFDT-2 flight was very successful in advancing the knowledge of supersonic decelerator technology, both in advancing inflatable decelerators with the successful deployment and operation of the SIAD-R and ballute, and in the discovery of a troubling disconnect between the subsonic and supersonic survivability of a Ringsail parachute.

Acknowledgments

The Low Density Supersonic Decelerator technology demonstration mission is sponsored by the National Aeronautics and Space Administration's Space Technology Mission Directorate. The authors thank the LDSD team across the participating government facilities and industrial contractors for helping to advance these technologies for the next generation of Mars landers.

A portion of the research described in this paper was carried out at the Jet Propulsion Laboratory, California Institute of Technology, under a contract with the National Aeronautics and Space Administration.

References

[1] Clark, I. G., Adler, M., Manning, R., "Summary of the First High-Altitude, Supersonic Flight Dynamics Test for the Low-Density Supersonic Decelerator Project," *23rd AIAA Aerodynamic Decelerator Systems Technology Conference and Seminar*, March 2015, Daytona Beach, FL, AIAA 2015-2100.

[2] Mayhue, R. J. and Eckstrom, C. V., "Flight-Test Results From Supersonic Deployment of an 18-Foot-Diameter (5.49-Meter) Towed Ballute Decelerator," NASA Technical Memorandum, TM X-1773, May 1969.

[3] Usry, J., "Performance of a Towed 48-Inch-Diameter (121.92-cm) Ballute Decelerator Tested in Free Flight at Mach Numbers From 4.2 to 0.4," NASA Technical Note, TN D-4943, Feb. 1969.

[4] Thompson, N. B., Karp, A. C., Gallon, J. C., Tanner, C. L., "Pyrotechnically Actuated Gas Generator Utilizing Aqueous Methanol," *23rd AIAA Aerodynamic Decelerator Systems Technology Conference and Seminar*, March 2015, Daytona Beach, FL, AIAA 2015-2115.

[5] Brandeau, E., Clark, I., Ginn, J., Tanner, C., "Ballutes for Supersonic Deceleration at Mars," IEEE Aerospace Conference, IEEEAC Paper 2551, Big Sky, MT, 2015.

[6] Meacham, M., Gallon, J., Johnson, M., Natzic, D., Thompson, N., Aguillar, D., Marti, B., Hennings, E., "Rocket Sled Strength Testing of Large, Supersonic Parachutes," *23rd AIAA Aerodynamic Decelerator Systems Technology Conference and Seminar*, March 2015, Daytona Beach, FL, AIAA 2015-2163.

[7] Gwinn, K., Totten, J., Waye, D., "High Strain-Rate Testing of Parachute Materials," *13th AIAA Aerodynamic Decelerator Systems Technology Conference and Seminar*, Clearwater Beach, FL, AIAA 1995-1546.

BIOGRAPHY

Ian Clark *is a Systems Engineer at NASA's Jet Propulsion Laboratory, a specialist in the area of Planetary Entry, Descent, and Landing (EDL), and is the Principal Investigator of NASA's Low-Density Supersonic Decelerator (LDSD) Project. Dr. Clark is the recipient of a number of awards including the Presidential Early Career Award for Scientists and Engineers, the JPL Lew Allen Award, and the JPL Explorer Award. He holds B.S., M.S., and Ph.D. degrees in Aerospace Engineering from the Georgia Institute of Technology, where he also previously served as a Visiting Assistant Professor and managed the EDL research group.*

Mark Adler *is the Project Manager for LDSD at NASA's Jet Propulsion Laboratory. He is a JPL Fellow and an AIAA Associate Fellow. At JPL he has been the Cassini Lead Mission Engineer, the Mars Exploration Program Architect, the Mars Sample Return Chief Engineer, and the Mars Exploration Rover Spirit Mission Manager. He holds a B.A. in Mathematics and an M.S. in Electrical Engineering from the University of Florida, and a Ph.D. in Physics from the California Institute of Technology.*